a0005

4.16 Electronic Properties of Alkanethiol Molecular Junctions: Conduction Mechanisms, Metal–Molecule Contacts, and Inelastic Transport

G Wang, T-W Kim, and T Lee, Gwangju Institute of Science and Technology, Gwangju, Korea

W Wang, University of Wyoming, Laramie, WY, USA

M A Reed, Yale University, New Haven, CT, USA

s0005

4.16.1 Introduction

p0005 Molecular electronics utilizing functional molecules as the ultimate nanoscale electronic components has recently generated considerable interest in both the basic transport physics of molecular systems and potential technological applications in a variety of functional electronic device components for ultra-high density future electronics [1–4].

p0010 However, despite the numerous potential advantages of molecular electronics as compared to traditional silicon-based electronics, there are many issues and challenges that need to be overcome to apply molecules to actual electronic circuits. For example, some reports of molecular mechanisms in electronic devices [3a,5,6a,b] have been shown to be premature due to filamentary conduction [3c,7], highlighting the fabrication sensitivity of molecular structures and the need to institute reliable controls and methods to validate true molecular transport [8]. A related problem is the characterization of molecules in the active device structures, including their configuration, bonding, and indeed even their very presence. In addition, metal–molecule contact is important not only for understanding the transport properties of molecular devices but also for realizing reproducible molecular electronic devices due to its role in controlling metal–molecule interfaces [9,10].

p0015 Here we present results on well-understood molecular assemblies, which exhibit an understood classical transport behavior, and which can be used as a control for eliminating (or understanding) fabrication variables. Utilizing tunneling spectroscopic methods, we present the unambiguous evidence of the presence of molecules in the junction. Using the statistical analysis on the current–voltage

characteristics of molecular junctions, we investigate the effect of metal–molecule contacts and present the contact resistances of the junctions.

p0020 A molecular system whose structure and configuration are sufficiently well characterized such that it can serve as a standard is the extensively studied alkanethiol self-assembled monolayer (SAM) [11]. There are two kinds of alkanethiols: alkanemomothiols ($CH_3(CH_2)_{n-1}SH$), where there is one thiol at an end of molecule; and alkanedithiols ($HS(CH_2)_nSH$), where there are thiols at both end of molecule. This molecule system is useful as a control since properly prepared SAMs form single van der Waals crystals [11,12], and presents a simple classical metal–insulator–metal (M-I-M) tunnel junction when fabricated between metallic contacts due to the large gap of approximately 8 eV[13–15] between the highest occupied molecular orbital (HOMO) and the lowest unoccupied molecular orbital (LUMO).

p0025 Various surface analytical tools have been utilized to investigate the surface and bulk properties of the alkanethiol SAMs, such as X-ray photoelectron spectroscopy [16], Fourier transform infrared spectroscopy (FTIR) [17], Raman spectroscopy [18], scanning tunneling microscopy (STM) [12], etc. For example, studies have shown that the bonding of the thiolate group to the gold surface is strong with a bonding energy of ~1.7 eV [11]. STM topography examinations revealed that alkanethiols adopt the commensurate crystalline lattice characterized by a $c(4\times2)$ superlattice of a $(\sqrt{3}\times\sqrt{3})R30°$ [12,19]. FTIR investigation showed that the orientation of the alkanethiol SAMs on Au(111) surfaces are tilted ~30° from the surface normal [20].

p0030 Electronic transport through alkanethiol SAMs have also been characterized by STM [21,22], conducting atomic force microscopy [23–26], mercury-drop junctions [29–30], cross-wire junctions [31], and electrochemical methods [32–34]. These investigations are exclusively at ambient temperature – clearly useful – but insufficient for an unambiguous claim that the transport mechanism is tunneling (of course expected, assuming that the Fermi levels of the contacts lie within the large HOMO–LUMO gap). However, in the absence of temperature-dependent current–voltage ($I(V,T)$) characteristics, other conduction mechanisms (e.g., thermionic, hopping, or filamentary conduction) cannot be excluded complicate the analysis, and thus such a claim is premature.

p0035 Utilizing a solid-state device structure that incorporates alkanethiol SAMs, we demonstrate devices that allow $I(V,T)$ and structure-dependent measurements [35,36] with results that can be compared with accepted theoretical models of M-I-M tunneling. The use of this fabrication approach is not special in any way (other than that we have so far found it to be successful) – indeed we stress that any successful device fabrication method should yield the results described below if one is characterizing the intrinsic molecular transport properties.

p0040 The electronic transport is further investigated with the technique of inelastic electron tunneling spectroscopy (IETS) [36]. IETS was developed in the 1960s as a powerful spectroscopic tool to study the vibrational spectrum of organic molecules confined inside metal-oxide–metal junctions [37–41]. In our study, IETS is utilized for the purpose of molecule identification, chemical bonding, and conduction mechanism investigations of the 'control' SAMs. The exclusive presence of well-known vibrational modes of the alkanes used are direct evidence of the molecules in the device structure, something that has to date only been inferred (with good reason, but nonetheless not unambiguously). The vibrational modes, exclusively identified as alkanes (as well as contact modes) are difficult to interpret in any other way other than as components in the active region of the device. The inelastic tunneling spectra also demonstrate that electronic tunneling occurs through the molecules, confirming the conduction mechanism obtained by $I(V,T)$ characterizations. The specific spectral lines also yield intrinsic linewidths that may give insight into molecular conformation, and may prove to be a powerful tool in future molecular device characterization.

p0045 We also present the influence of metal–molecule contacts in molecular junctions using a proposed multibarrier tunneling (MBT) model where the metal–molecule–metal junction can be divided into three parts: the molecular-chain body with metal–molecule contacts on either side of molecule [9,10]. The MBT model will help introduce an insight for studying charge transport mechanisms, focused on the metal–molecule contacts in molecular electronic devices or other nanoscale devices.

4.16.2 Experiment s0010

p0050 Electronic transport measurements on alkanethiol SAMs were performed using two different device structures. The first device structure is similar to the nanoscale device structure reported previously, the so-called 'nanopore' devices [3a,35,36,42–44].

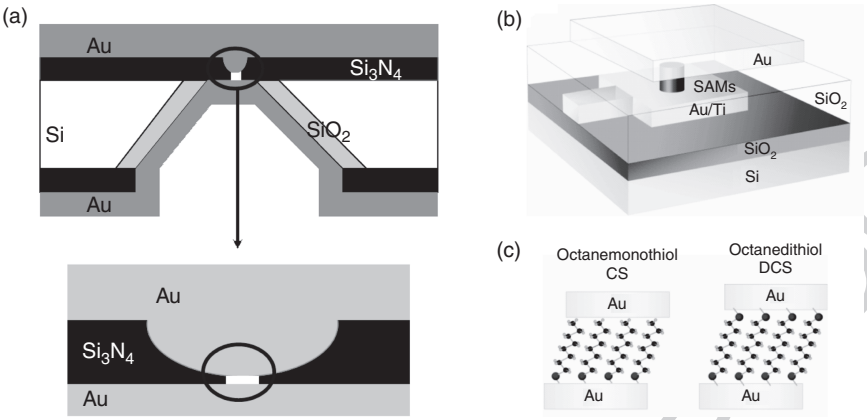

f0005 **Figure 1** (a) Schematics of a nanometer scale device used in this study (not drawn to scale in the relative thickness). Top schematic is the cross section of a silicon wafer with a nanometer scale pore etched through a suspended silicon nitride membrane. Middle and bottom schematics show a Au/SAM/Au junction formed in the pore area. (b) Schematics of microscale via-hole junctions used in this study. (c) The structures of octanethiol and octanedithiol are shown as examples.

Another device structure is vertical metal–molecule–metal device structure with microscale via-holes [9,10,45].

p0055 In the nanopore devices, as illustrated in **Figure 1(a)** (not drawn to scale in the relative thickness), a number of molecules (several thousands) are sandwiched between two metallic contacts. This technique provides a stable device structure and makes cryogenic measurements possible. The device fabrication starts with a high-resistivity silicon wafer with low-stress Si_3N_4 film deposited on both sides by low-pressure chemical vapor deposition (LPCVD). By standard photolithography processing, a suspended Si_3N_4 membrane (size of 40 μm×40 μm and thickness of ~70 nm) is fabricated on the topside of the wafer. Subsequent e-beam lithography and reactive ion etching creates a single pore with a diameter of tens of nanometers through the membrane. As the next step, 150 nm gold is thermally evaporated onto the topside of the wafer to fill the pore and form one of the metallic contacts.

p0060 The device is then transferred into a molecular solution to deposit the SAM layer. For our experiments, a ~5 mM alkanethiol solution is prepared by adding ~10 μl alkanethiols into 10 ml ethanol [46]. The deposition is done in solution for 24 h inside a nitrogen-filled glove box with an oxygen level of less than 100 ppm. Alkanemonothiols and alkanedithiols of different molecular lengths: octanemonothiol ($CH_3(CH_2)_7SH$, C8), dodecanemonothiol ($CH_3(CH_2)_{11}SH$, C12), hexadecanemonothiol ($CH_3(CH_2)_{15}SH$, C16), octanedithiol ($HS(CH_2)_8SH$, DC8), nonanedithiol ($HS(CH_2)_9SH$, DC9), and decanedithol ($HS(CH_2)_{10}SH$, DC10) were used to form the active molecular components in molecular devices [46]. As representative examples, the chemical structures of octanethiol and octanedithiol are shown in **Figure 1(c)**.

p0065 In order to statistically determine the pore size in nanopore devices, test patterns (arrays of pores) were created under similar fabrication conditions. This indirect measurement of device size is done since SEM examination of the actual device can cause hydrocarbon contamination of the device and subsequent contamination of the monolayer. From regression analysis of 298 pores, the device sizes of the C8, C12, C16, and C8-dithiol samples are determined as 50 ± 8, 45 ± 2, 45 ± 2, and 51 ± 5 nm in diameters, respectively. A more ideal (less parasitic) C8 sample supercedes that of previous reports [35], and derived parameters from the two data sets agree to within a standard error. We will use these device areas as the effective contact areas. Although one could postulate that the actual area of metal that contacts the molecules may be different, there is little reason to propose that it would be different as a function of length over the range of alkanethiols used, and at most would be a constant systematic error.

p0070 The other device structure is shown in **Figure 1(b)**, that is, a vertical metal–molecule–metal junction device structure having a micrscale via-hole in which the molecules are self-assembled.

p0075 The sample is then transferred in ambient conditions to an evaporator that has a cooling stage to deposit the opposing Au contact in case of both device structures. During the thermal evaporation (under the pressure of 10^{-7}–10^{-8} Torr), liquid

nitrogen is kept flowing through the cooling stage in order to avoid thermal damage to the molecular layer [35,47]. This technique reduces the kinetic energy of evaporated Au atoms at the surface of the monolayer, thus preventing Au atoms from punching through the monolayer. For the same reason, the evaporation rate is kept very low. The deposition rate is typically 0.1–0.5 Å s^{-1}. A total of 50–200 nm gold is deposited to form the contact.

p0080 The device is subsequently packaged and loaded into a low-temperature cryostat. The sample temperature is varied from 300 to 4.2 K by flowing cryogen vapor onto the sample (and thermometer) using a closed-loop temperature controller. Two-terminal direct current (DC) $I(V)$ measurements are performed using a semiconductor parameter analyzer. Inelastic electron tunneling spectra are obtained via a standard lock-in second harmonic measurement technique [37,38]. A synthesized function generator is used to provide both the modulation and the lock-in reference signal. The second harmonic signal (proportional to d^2I/dV^2) is directly measured using a lock-in amplifier, which is checked to be consistent with a numerical derivative of the first-harmonic signal (proportional to dI/dV). Various modulation amplitudes and frequencies are utilized to obtain the spectra. The alternating current (AC) modulation is added to a DC bias using operational amplifier-based custom circuitry [48].

s0015 4.16.3 Theoretical Basis

s0020 4.16.3.1 Possible Conduction Mechanisms

p0085 In **Table 1**, possible conduction mechanisms are listed with their characteristic current, temperature, and voltage dependencies [49] (we do not discuss filamentary tunneling mechanisms, which are easier to categorize[50a–c]). Based on whether thermal activation is involved, the conduction mechanisms fall into two distinct categories: (i) thermionic or hopping conduction, which has temperature-dependent $I(V)$ behavior and (ii) direct tunneling or Fowler–Nordheim tunneling, which does not have temperature-dependent $I(V)$ behavior. For example, thermionic and hopping conductions have been observed for 4-thioacetylbiphenyl SAMs[42] and 1,4-phenelyene diisocyanide SAMs [43b]. On the other hand, the conduction mechanism is expected to be tunneling when the Fermi levels of contacts lie within the large HOMO–LUMO gap for short-length molecule, as for the case of alkanethiol molecular system [13–15]. Previous work on Langmuir–Blodgett alkane monolayers[51a,b] exhibited a significant impurity-dominated transport component, complicating the analysis. The $I(V)$ measurements on self-assembled alkanethiol monolayers have also been reported [21–31,52]; however, all of these measurements were performed at fixed temperature (300 K), which is insufficient to prove tunneling as the dominant mechanism.

4.16.3.2 Tunneling Models s0025

To describe the transport through a molecular system having HOMO and LUMO energy levels, one of the applicable models is the Franz two-band model [53–56]. This model provides a nonparabolic energy–momentum $E(k)$ dispersion relationship by considering the contributions of both the HOMO and LUMO energy levels [53]: p0090

$$k^2 = \frac{2m^*}{\hbar^2} E\left(1 + \frac{E}{E_g}\right) \quad (1)$$

t0005 **Table 1** Possible conduction mechanisms

Conduction mechanism	*Characteristic Behavior*	*Temperature dependence*	*Voltage dependence*
Direct tunneling[a]	$J \sim V\exp\left(-\frac{2d}{\hbar}\sqrt{2m\Phi}\right)$	None	$J \sim V$
Fowler–Nordheim tunneling	$J \sim V^2\exp\left(-\frac{4d\sqrt{2m}\Phi^{3/2}}{3q\hbar V}\right)$	None	$\ln\left(\frac{J}{V^2}\right) \sim \frac{1}{V}$
Thermiomic emission	$J \sim T^2\exp\left(-\frac{\Phi - q\sqrt{qV/4\pi\varepsilon d}}{kT}\right)$	$\ln\left(\frac{J}{T^2}\right) \sim \frac{1}{T}$	$\ln(J) \sim V^{1/2}$
Hopping conduction	$J \sim V\exp\left(-\frac{\Phi}{kT}\right)$	$\ln\left(\frac{J}{V}\right) \sim \frac{1}{T}$	$J \sim V$

[a] This characteristic of direct tunneling is valid for the low bias regime (see **equation 3a**).
Adapted with permission from Sze SM (1981) *Physics of Semiconductor Devices*. New York: Wiley.

where k is the imaginary part of wave vector of electrons, m^* the electron effective mass, h $(=2\pi\hbar)$ the Planck's constant, E the electron energy, and E_g the HOMO–LUMO energy gap. From this nonparabolic $E(k)$ relationship, the effective mass of the electron tunneling through the SAM can be deduced by knowing the barrier height of the metal–SAM–metal junction.

p0095 When the Fermi level of the metal is aligned close enough to one energy level (either HOMO or LUMO), the effect of the other distant energy level on the tunneling transport is negligible, and the widely used Simmons model [57] is an excellent approximation. Simmons model expressed the tunneling current density through a barrier in the tunneling regime of $V < \Phi_B/e$ as [27,57]

$$\mathcal{J}=\left(\frac{e}{4\pi^2\hbar d^2}\right)\left\{\left(\Phi_B-\frac{eV}{2}\right)\exp\left[-\frac{2(2m)^{1/2}}{\hbar}\alpha\left(\Phi_B-\frac{eV}{2}\right)^{1/2}d\right]-\left(\Phi_B+\frac{eV}{2}\right)\exp\left[-\frac{2(2m)^{1/2}}{\hbar}\alpha\left(\Phi_B+\frac{eV}{2}\right)^{1/2}d\right]\right\} \quad (2)$$

where m is the electron mass, d the barrier width, Φ_B the barrier height, and V the applied bias. For molecular systems, the Simmons model has been modified with a parameter α [27,35]. Here α is a unitless adjustable parameter that is introduced to provide either a way of applying the tunneling model of a rectangular barrier to tunneling through a nonrectangular barrier [27], or an adjustment to account for the effective mass (m^*) of the tunneling electrons through a rectangular barrier [27,35,56,58], or both. Here $\alpha = 1$ corresponds to the case for a rectangular barrier and bare electron mass. By fitting individual $I(V)$ data using equation 2, Φ_B and α values can be obtained.

p0100 **Equation 2** can be approximated in two limits: low bias and high bias as compared with the barrier height Φ_B. For the low bias range, **equation 2** can be approximated as [57]

$$\mathcal{J}\approx\left(\frac{(2m\Phi_B)^{1/2}e^2\alpha}{h^2 d}\right)V\exp\left[-\frac{2(2m)^{1/2}}{\hbar}\alpha(\Phi_B)^{1/2}d\right] \quad (3a)$$

p0105 To determine the high bias limit, we compare the relative magnitudes of the first and second exponential terms in **equation 2**. At high bias, the first term is dominant and thus the current density can be approximated as

$$\mathcal{J}\approx\left(\frac{e}{4\pi^2\hbar d^2}\right)\left(\Phi_B-\frac{eV}{2}\right)\times\exp\left[-\frac{2(2m)^{1/2}}{\hbar}\alpha\left(\Phi_B-\frac{eV}{2}\right)^{1/2}d\right] \quad (3b)$$

The tunneling currents in both bias regimes are exponentially dependent on the barrier width d. In the low-bias regime the tunneling current density is $\mathcal{J}\propto(1/d)\exp(-\beta_0 d)$, where β_0 is bias-independent decay coefficient: p0110

$$\beta_0=\frac{2(2m)^{1/2}}{\hbar}\alpha(\Phi_B)^{1/2} \quad (4a)$$

while in the high-bias regime, $\mathcal{J}\propto(1/d)^2\exp(-\beta_V d)$, where β_V is bias-dependent decay coefficient:

$$\beta_V=\frac{2(2m)^{1/2}}{\hbar}\alpha\left(\Phi_B-\frac{eV}{2}\right)^{1/2}=\beta_0\left(1-\frac{eV}{2\Phi_B}\right)^{1/2} \quad (4b)$$

At high bias, β_V decreases as bias increases, which results from barrier-lowering effect due to the applied bias.

4.16.4 Results s0030

4.16.4.1 Tunneling Current–Voltage Characteristics s0035

4.16.4.1.1 Temperature–variable current–voltage (I(V,T)) measurement s0040

In order to determine the conduction mechanism of self-assembled alkanethiol molecular systems $I(V)$ measurements in a sufficiently wide temperature range (300 to 80 K) and resolution (10 K) were performed. **Figure 2(a)** shows a representative $I(V,T)$ characteristic of dodecanemonothiol (C12) measured with the device structure as shown in **Figure 1(a)**. Positive bias corresponds to electrons injected from the physisorbed Au contact (bottom contact in **Figure 1(a)**) into the molecules. By using the contact area of 45 ± 2 nm in diameter determined from SEM study, a current density of 1500 ± 200 A cm^{-2} at 1.0 V is determined. No significant temperature dependence of the characteristics (from $V = 0$–1.0 V) is observed over the range from 300 to 80 K. An Arrhenius plot ($\ln(I)$ versus $1/T$) of this is shown in **Figure 2(b)**, exhibiting little temperature dependence in the slopes of $\ln(I)$ versus $1/T$ at different bias and thus indicating the absence of thermal activation. Therefore, we conclude that the conduction mechanism through alkanethiol is tunneling contingent on demonstrating a correct molecular length dependence. p0115

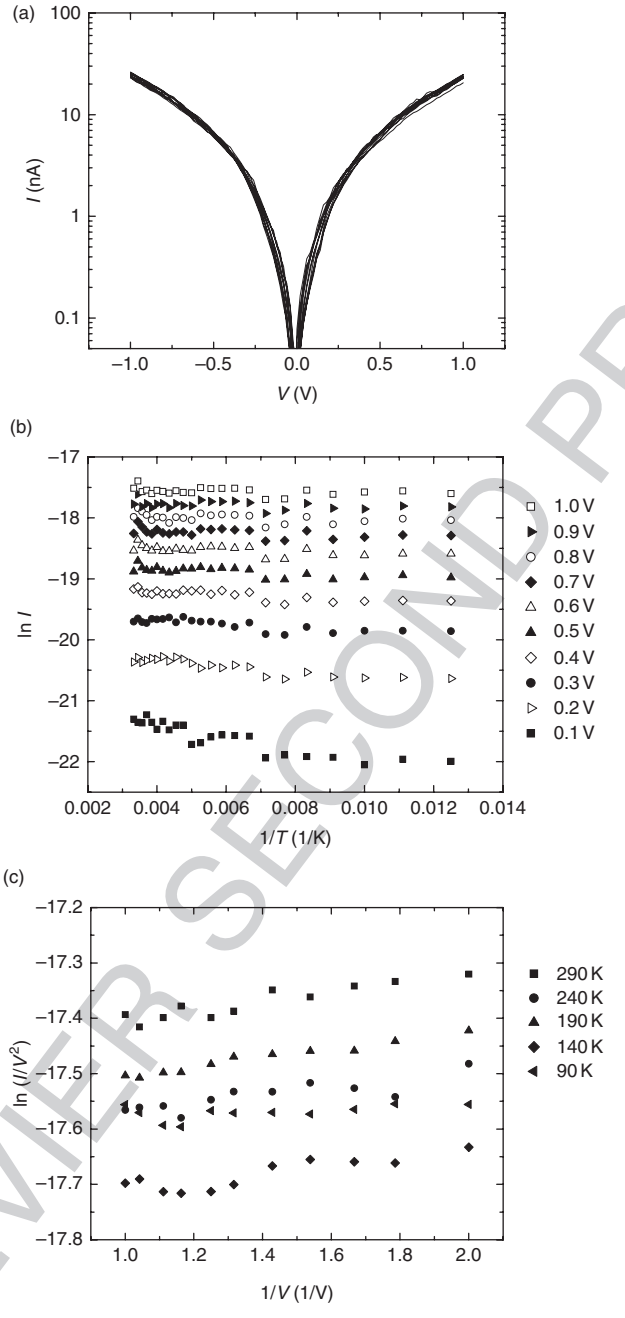

f0010 **Figure 2** (a) Temperature-dependent $I(V)$ characteristics of dodecanethiol (C12). $I(V)$ data at temperatures from 300 to 80 K with 20 K steps are plotted on a log scale. (b) Arrhenius plot generated from the $I(V)$ data in (a), at voltages from 0.1 to 1.0 V with 0.1 V steps. (c) Plot of $\ln(I/V^2)$ versus $1/V$ at selected temperatures.

The tunneling through alkanethiol SAMs has been assumed as 'through-bond' tunneling, that is, along the tilted molecular chains between the metal contacts [24,25,34,59a,b]. Based on the applied bias as compared with the barrier height (Φ_B), the tunneling through an SAM layer can be categorized into either direct ($V < \Phi_B/e$) or Fowler–Nordheim ($V > \Phi_B/e$) tunneling. These two tunneling mechanisms can be distinguished due to their distinct voltage dependencies (see **Table 1**). Analysis of $\ln(I/V^2)$ versus $1/V$ [in **Figure 2(c)**] shows no significant voltage dependence, indicating no obvious Fowler–Nordheim transport behavior in this bias range (0 to 1.0 V) and thus determining that the barrier height is larger than

the applied bias, that is, $\Phi_B > 1.0\,eV$. This study is restricted to applied biases $\leq 1.0\,V$ and the transition from direct to Fowler–Nordheim tunneling requires higher bias.

p0120 The importance of variable temperature measurements to validate tunneling is demonstrated in **Figure 3**. Here the $I(V)$ of an octanemonothiol (C8) device is shown (**Figure 3(a)**), whose $I(V)$ shape looks very similar to **Figure 2** (i.e., direct tunneling), and indeed can be fit to a Simmons model. However, further $I(V,T)$ measurements display an obvious temperature dependence (**Figure 3(b)**), which can be fit well to a hopping conduction model (**Table 1**) with a well-defined activation energy of 190 meV (**Figure 3(c)**). This and other similar impurity-mediated transport phenomena (such as Coulomb blockade) are observed in a subset of devices and is indicative of the unintentional incorporation of a trap or defect level in those devices. This study instead focuses on devices that do not show any defect-mediated transport and probes the intrinsic behavior of the molecular layer.

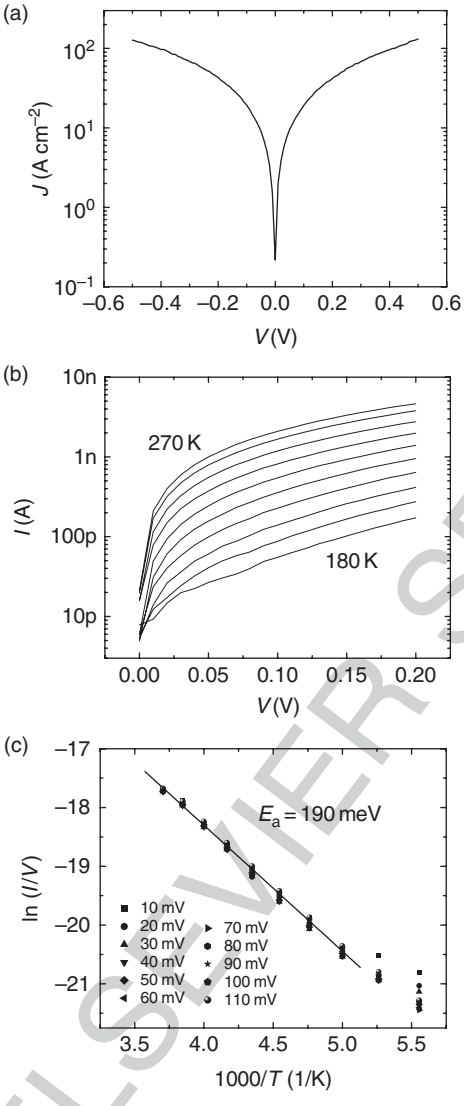

f0015 **Figure 3** (a) $I(V)$ characteristics of an octanethiol (C8) device at 270 K. (b) Temperature dependence of the device from 270 to 180 K (in 10 K increments). (c) Plot of ln(I/V) versus $1/T$ at various voltages. The activated behavior is independent of bias voltage; thus, the behavior is hopping (in this device) due to incorporation of a defect of energy 190 meV. This class of devices is not suitable for investigation of the intrinsic transport mechanism in the SAM as it is dominated by a defect.

Having established tunneling as the conduction mechanism in a device, we will now obtain the barrier height by comparing experimental $I(V)$ data with theoretical calculations from tunneling models. p0125

4.16.4.1.2 Tunneling characteristics through alkanethiols s0045

From the modified Simmons model (**equation 2**) by adjusting two parameters Φ_B and α, a nonlinear least-squares fitting can be performed to fit the measured C12 $I(V)$ data (calculation assuming $\alpha = 1$ has been previously shown not to fit $I(V)$ data well for some alkanethiol measurements at fixed temperature (300 K)) [27]. By using a device size of 45 nm in diameter, the best-fitting parameters (minimizing χ^2) for the room temperature C12 $I(V)$ data were found to be $\Phi_B = 1.42 \pm 0.04\,eV$ and $\alpha = 0.65 \pm 0.01$, where the error ranges of Φ_B and α are dominated by potential device size fluctuations of 2 nm. Likewise, data sets were obtained and fittings were done for octanethiol (C8) and hexadecanethiol (C16), which yielded values ($\Phi_B = 1.83 \pm 0.10\,eV$ and $\alpha = 0.61 \pm 0.01$) and ($\Phi_B = 1.40 \pm 0.03\,eV$, $\alpha = 0.68 \pm 0.01$), respectively. p0130

Using $\Phi_B = 1.42\,eV$ and $\alpha = 0.65$, a calculated $I(V)$ for C12 is plotted as a solid curve in a linear scale (**Figure 4(a)**) and in a semi-log scale (**Figure 4(b)**). A calculated $I(V)$ for $\alpha = 1$ and $\Phi_B = 0.65\,eV$ (which gives the best fit at low-bias range) is shown as the dashed curve in the same figure, illustrating that with $\alpha = 1$ only limited regions of the $I(V)$ can be fit (specifically here, for $V < 0.3\,V$). For the case of a rectangular barrier, the α parameter fit presented above corresponds to an effective mass m^* ($= \alpha^2 m$) of $0.42m$. p0135

In order to investigate the dependence of the Simmons model fitting on Φ_B and α, a fitting minimization analysis was undertaken on the individual Φ_B p0140

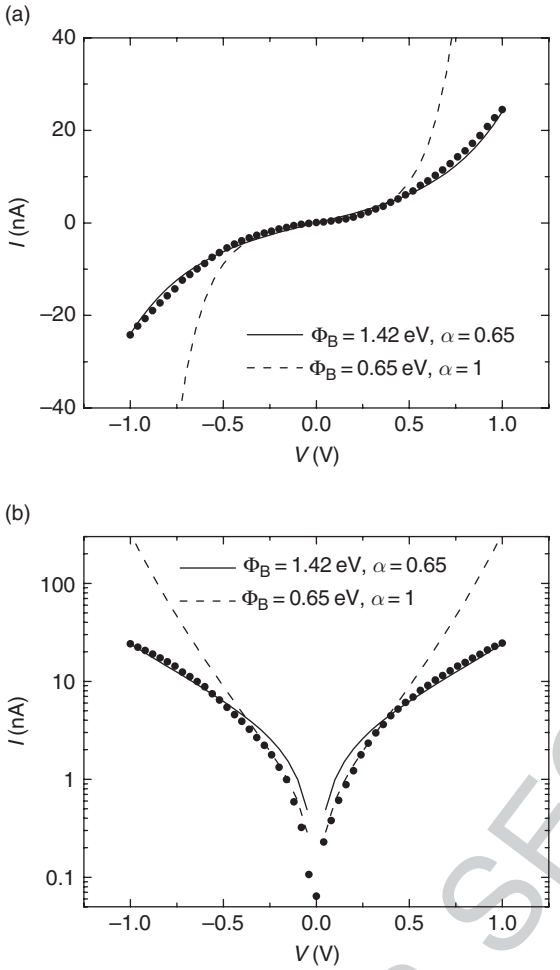

f0020 **Figure 4** Measured C12 *I*(*V*) data (circular symbols) is compared with calculation (solid curve) using the optimum fitting parameters of $\Phi_B = 1.42$ eV and $\alpha = 0.65$. The calculated *I*(*V*) from a simple rectangular model ($\alpha = 1$) with $\Phi_B = 0.65$ eV is also shown as the dashed curve. Current is plotted (a) on linear scale and (b) on log scale.

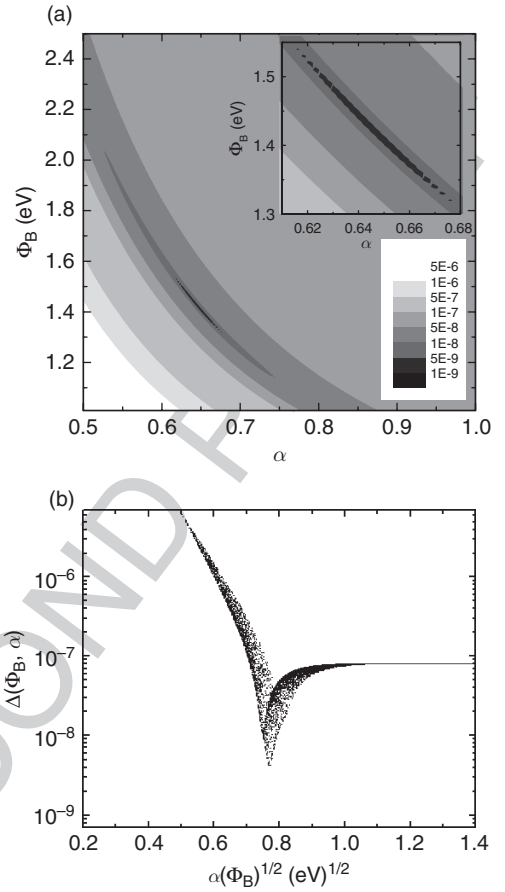

Figure 5 (a) Contour plot of $\Delta(\Phi_B, \alpha)$ values for C12 nanopore device as a function of Φ_B and α, where the darker region corresponds to a better fitting. Inset shows detailed minimization fitting regions. (b) A plot of $\Delta(\Phi_B, \alpha)$ as a function of $\alpha\Phi_B{}^{1/2}$. f0025

and α values as well as their product form of $\alpha\Phi_B^{1/2}$ in **equation 4a**. The quantity $\Delta(\Phi_B, \alpha) = \left(\sum \left|I_{\exp,v} - I_{cal,v}\right|^2\right)^{1/2}$ was calculated and plotted where $I_{\exp,V}$ is the experimental current–voltage values and $I_{\mathrm{cal},V}$ is calculated using **equation 2**. Seven thousand five hundred different $\{\Phi_B, \alpha\}$ pairs were used in the fittings with Φ_B ranging from 1.0 to 2.5 eV (0.01 eV increment) and α from 0.5 to 1.0 (0.01 increment). **Figure 5(a)** is a representative contour plot of $\Delta(\Phi_B, \alpha)$ versus Φ_B and α values generated for the C12 *I*(*V*) data, where darker regions correspond to smaller $\Delta(\Phi_B, \alpha)$ and various shades represent half order of magnitude $\Delta(\Phi_B, \alpha)$ steps. The darker regions represent better fits of **equation 2** to the measured *I*(*V*) data. In the inset in **Figure 5(a)** one can see there is a range of possible Φ_B and α values yielding minimum fitting parameters. Although the tunneling parameters determined from the previous Simmons tunneling fitting ($\Phi_B = 1.42$ eV and $\alpha = 0.65$) lie within this minimum region in this figure, there is a distribution of other possible values.

A plot of $\Delta(\Phi_B, \alpha)$ versus $\alpha\Phi_B{}^{1/2}$ for the same p0145 device reveals a more pronounced dependence, and is shown in **Figure 5(b)**. This plot indicates the fitting to the Simmons model sharply depends on the product of $\alpha\Phi_B{}^{1/2}$. For this plot the $\Delta(\Phi_B, \alpha)$ is minimized at $\alpha\Phi_B{}^{1/2}$ of 0.77 $(eV)^{1/2}$ corresponding to a β_0 value of 0.79 $\mathring{A}^{-1}$ from **equation 4a**. The C8 and C16 devices showed similar results, indicating the Simmons tunneling model has a strong $\alpha\Phi_B{}^{1/2}$

t0010 **Table 2** Summary of alkanethiol tunneling parameters in this study

Molecules	*J at 1 V (A cm^{-2})*	Φ_B *(eV)*	α	*m*[a] *(m)*	β_0 *(Å^{-1})*[a]
C8	31 000 ± 10 000	1.83 ± 0.10	0.61 ± 0.01	0.37	0.85 ± 0.04
C12	1500 ± 200	1.42 ± 0.04	0.65 ± 0.01	0.42	0.79 ± 0.02
C16	23 ± 2	1.40 ± 0.03	0.68 ± 0.01	0.46	0.82 ± 0.02
C8-dithiol	93 000 ± 18 000	1.20 ± 0.03	0.59 ± 0.01	0.35	0.66 ± 0.02

[a] β_0 values were calculated using **equation 4a**.

dependence. For the C8 device, although Φ_B obtained from the fitting is a little larger, combined α and Φ_B gives a similar β_0 value within the error range as the C12 and C16 devices (**Table 2**).

s0050 ***4.16.4.1.3 Length-dependent tunneling through alkanethiols***

p0150 Three alkanemonothiols of different molecular length (C8, C12, and C16) were investigated to study the length-dependent tunneling behavior. **Figure 6** is a semi-log plot of tunneling current densities multiplied by molecular length ($\mathcal{J}d$ at low bias and $\mathcal{J}d^2$ at high bias) as a function of the molecular length for these alkanethiols. The molecular lengths used in this plot are 13.3, 18.2, and 23.2 Å for C8, C12, and C16, respectively. Each molecular length was determined by adding an Au-thiol bonding length to the length of molecule [24]. Note that these lengths assume through-bond tunneling [24,25,34,59a,b]. The high- and low-bias regimes are defined somewhat arbitrarily by comparing the relative magnitudes of the first and second exponential terms in **equation 2**. Using $\Phi_B = 1.42$ eV and $\alpha = 0.65$ obtained from nonlinear least-squares fitting of the C12 $I(V)$ data, the second term becomes less than ~10 % of the first term at ~0.5 V that is chosen as the boundary of low- and high-bias ranges.

As seen in **Figure 6**, the tunneling current shows p0155 exponential dependence on molecular length, which is consistent with the Simmons tunneling model (**equation 3**). The β values can be determined from the slope at each bias and are plotted in **Figure 7**. The error bar of an individual β value in this plot was obtained by considering both the device size uncertainties and the linear-fitting errors.

The β values determined are almost independent p0160 of bias in the low-bias range ($V < \sim 0.5$ V), and an average β of 0.77 ± 0.06 Å^{-1} in this region (from 0 to 0.5 V) can be calculated from **Figure 7**. **Table 3** is a summary of previously reported alkanethiol transport parameters obtained by different techniques. The current densities ($\mathcal{J}$) listed in **Table 3** are for C12 monothiol or dithiol devices at 1 V, which are extrapolated from published results of other length alkane molecules. The large variation of $\mathcal{J}$ of these reports can be attributed to the uncertainties in device contact geometry and junction area, as well as complicating inelastic or defect contributions. The β value (0.77 ± 0.06 Å^{-1} ≈ 0.96 ± 0.08 per methylene) for alkanethiols reported here is comparable

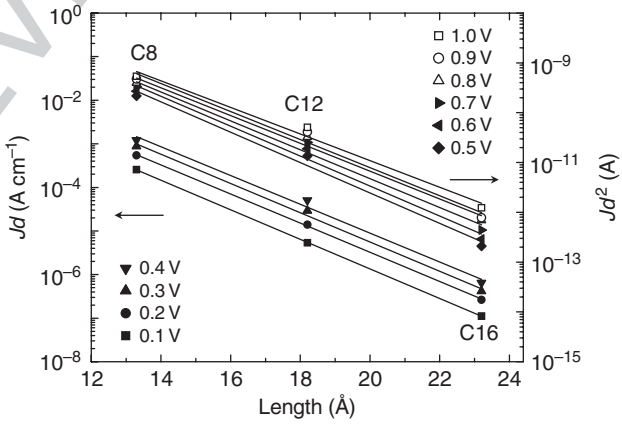

f0030 **Figure 6** Log plot of tunneling current densities multiplied by molecular length d at low bias and by d^2 at high bias (symbols) versus molecular lengths. The lines through the data points are linear fittings.

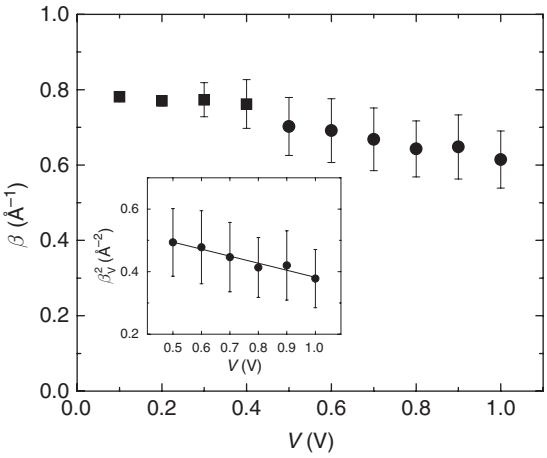

f0035 **Figure 7** Plot of β versus bias in the low-bias range (square symbols) and high-bias ranges (circular symbols). The inset shows a plot of β_V^2 versus bias with a linear fitting.

to previously reported values as summarized in **Table 3**. This β value agrees with the value of 0.79 $Å^{-1}$ (β_0) calculated via **equation 4a** from fitting individual $I(V)$ characteristic of the C12 device. The calculated β_0 of C8 and C16 devices also have similar values, as summarized in **Table 2**.

p0165 According to **equation 4b**, β_V^2 depends on bias V linearly in the high-bias range. The inset in **Figure 7** is a plot of β_V^2 versus V in this range (0.5 to 1.0 V) along with linear fitting of the data. From this fitting, $\Phi_B = 1.35 \pm 0.20$ eV and $\alpha = 0.66 \pm 0.04$ were obtained from the intercept and the slope, respectively, consistent with the values ($\Phi_B = 1.42$ eV and $\alpha = 0.65$) obtained from the nonlinear least-squares fitting in the previous section.

The β values for alkanethiols obtained by various p0170 experimental techniques have previously been reported and are summarized in **Table 3** [21–41,52]. In order to compare with these reported β values, we also performed a length-dependent analysis on our experimental data according to the generally used equation [22–30,35]:

$$G = G_0 \exp(-\beta d) \tag{5}$$

This gives a β value from 0.84 to 0.73 $Å^{-1}$ in the p0175 bias range from 0.1 to 1.0 V, which is comparable to results reported previously. For example, Holmlin *et al.* [27] reported a β value of 0.87 $Å^{-1}$ by mercury drop experiments and Wold *et al.* [24] have reported β of 0.94 $Å^{-1}$ and Cui *et al.* [25] reported β of 0.64 $Å^{-1}$ for various alkanethiols by using a conducting atomic force microscope technique. These reported β were treated as bias-independent quantities, contrary to the results reported here and that observed in

t0015 **Table 3** Summary of alkanethiol tunneling characteristic parameters

Junction	β ($Å^{-1}$)	*J*(A cm^{-2}) *at 1 V*	Φ_B (eV)	*Technique*	*Ref.*
(Bilayer) monothiol	0.87 ± 0.1	25–200[a]	2.1[e]	Hg-junction	[25]
(Bilayer) monothiol	0.71 ± 0.08	0.7–3.5[a]		Hg-junction	[27]
Monothiol	0.79 ± 0.01	1500 ± 200[b]	1.4[e]	Solid M-I-M	[33]
Monothiol	1.2			STM	[19]
Dithiol	0.8 ± 0.08	3.7–5 × 10^{5}[c]	5 ± 2[f]	STM	[20]
Monothiol	0.73 – 0.95	1100–1900[d]	2.2[e]	CAFM	[21]
Monothiol	0.64–0.8	10–50[d]	2.3[e]	CAFM	[23]
Dithiol	0.46 ± 0.02	3–6×10^{5}[c]	1.3–1.5[e]	CAFM	[24]
Monothiol	1.37 ± 0.03		1.8[f]	Tuning fork AFM	[49]
Monothiol	0.97 ± 0.04			Electrochemical	[30]
Monothiol	0.85			Electrochemical	[31]
Monothiol	0.91 ± 0.08			Electrochemical	[32]
Monothiol	0.76	2×10^{4} (at 0.1 V)[c]	1.3–3.4[g]	Theory	[58]
Monothiol	0.76			Theory	[59]
Monothiol	0.79			Theory	[56]

[a] The junction areas were estimated by optical microscope.
[b] The junction areas were estimated by SEM.
[c] The junction areas were estimated by assuming single molecule.
[d] The junction areas were estimated by assuming Hertzian contact theory.
[e] Barrier height Φ_B values were obtained from Simmons equation.
[f] Barrier height Φ_B values were obtained from bias dependence of β.
[g] Barrier height Φ_B values were obtained from a theoretical calculation.
Notes: Some decay coefficients β were converted into the unit of $Å^{-1}$ from the unit of per methylene. Current densities (*J*) for C12 monothiol or dithiol at 1 V are extrapolated from published results for other length molecules by using conductance $\propto \exp(-\beta d)$ relationship.

a slightly different alkane system (ligand-encapsulated nanoparticle/alkane-dithiol molecules) [26]. We also caution against the use of parameters that have not been checked with a temperature-dependent analysis, since small nontunneling components can dramatically affect derived values of β.

s0055 ***4.16.4.1.4 Franz model***

p0180 We have analyzed our experimental data using a Franz two-band model [53–56]. Since there are no reliable experimental data on the Fermi level alignment in these metal–SAM–metal systems, Φ_B and m^* are treated as adjustable parameters. We performed a least-squares fit on our data with the Franz nonparabolic $E(k)$ relationship (**equation 1**) using an alkanethiol HOMO–LUMO gap of 8 eV [14,15]. **Figure 8** shows the resultant $E(k)$ relationship and the corresponding energy band diagrams. The zero of energy in this plot was chosen as the LUMO energy. The best-fitting parameters obtained by minimizing χ^2 were $\Phi_B = 1.49 \pm 0.51$ eV and $m^* = 0.43 \pm 0.15m$, where the error ranges of Φ_B and m^* are dominated by the error fluctuations of β ($k^2 = -(\beta/2)^2$). Both electron tunneling near the LUMO and hole tunneling near the HOMO can be described by these parameters. The value of $\Phi_B = 1.49$ eV indicates that the Fermi level is aligned close to one energy level in either case; therefore, the Simmons model is a valid approximation. The Φ_B and m^* values obtained here are in reasonable agreement with the previous results obtained from the Simmons model.

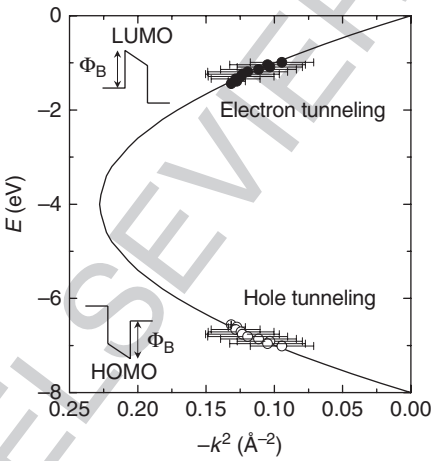

f0040 **Figure 8** $E(k)$ relationship (symbols) generated from the length-dependent measurement data for alkanethiols. Solid and open symbols correspond to electron and hole tunneling, respectively. The insets show the corresponding energy-band diagrams. The solid curve is the Franz two-band expression for $m^* = 0.43m$.

4.16.4.2 Metal–Molecule Contacts for Alkanethiols Junction s0060

4.16.4.2.1 Statistical analysis of contact properties through alkanethiols s0065

p0185 The yield of molecular electronic devices of even these robust alkanethiol molecular systems, however, is very low, mainly because of electrical shorts caused by the penetration of the top electrode through the molecular layer and making contact with the bottom electrode [8,60a,b]. A recent study, with the objective of preventing electrical shorts by using a layer of a highly conducting polymer resulted in a significant improvement in the yield of molecular electronic devices [61]. However, studies on the device yield of simple M-M-M junctions have not been extensive. In particular, systematic studies with the goal of defining 'working' molecular devices, device yield, and even selecting 'representative' devices have not been reported. Furthermore, determining the average transport parameters from a statistically meaningful number of molecular working devices is important, because the statistically averaged transport parameters can provide more accurate and meaningful characteristics of molecular systems. Statistical measurement has been performed, for example, to extract the electrical conductance of single molecules using mechanically controllable break junctions [62]. As mentioned above, the yields of the molecular electronic devices are very low, mainly due to electric short problems [8,60a,b,61]. However, thorough and systematic studies on what 'working' devices are and on the yields of the molecular electronic devices have not been reported. Typically, working devices might be defined as a device showing nonlinear $I(V)$ behavior and not being electrical open and short. Electrical open and short devices can be readily recognized. Open devices are noisy with a current level typically in the pA range and short devices show ohmic $I(V)$ characteristics with a current level larger than a few mA [63]. However, criteria are needed for determining working devices more precisely. Although the choice of such a criterion is not universal, current density can be a good criterion for determining working devices, because $I(V)$ data are major characteristics that are measured initially and the current directly reflects the conductivity of different lengths (or contacts) of alkanethiols or different molecular systems.

p0190 We fabricated and characterized a significantly large number of microscale molecular devices shown as **Figure 1(b)** (27 840 devices in total) to statistically analyze the molecular electronic

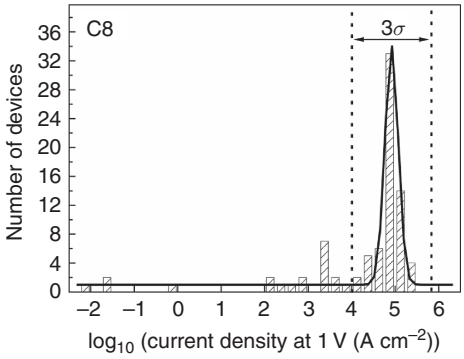

f0045 **Figure 9** Histogram of logarithmic current densities at 1 V for 'candidate' C8 molecular electronic devices. Solid lines are Gaussian fitting curves. (See text for the definition of candidate and working devices.)

properties of a sufficient number of 'working' molecular electronic devices (427 devices) [9,45].

p0195 The working devices displaying molecular properties were determined based on the statistical distribution of the current densities of the fabricated devices. Note that we selected the 99.7% of the devices by using the normal distribution function (Gaussian function) from the overall population, which are included in the interval of the 3σ range between $\mu+3\sigma$ and $\mu-3\sigma$, where μ is the average and σ is the standard deviation. When current densities are within the 3σ range (indicated as dotted lines in **Figure 9**), they are defined as working molecular electronic devices, whereas the others are defined as 'nonworking' devices when the current densities are out of this range. **Figure 9** shows an example of a histogram plot for logarithmic current densities of all C8 candidate devices. Similarly, we are able to define the working device ranges of alkanemonothiols and alkanedithiols devices. Basically, working molecular electronic devices were extracted from devices showing a majority of current densities in the statistical distribution. As summarized in **Table 4**, the numbers of C8, C12, C16, DC8, DC9, and DC10 working devices were 63, 33, 60, 84, 94, and 93, respectively, among the total 27 840 fabricated devices. Then, the device yields were found as ~1.2% (156/13 440) for monothiol and ~1.9% (271/14 440) for dithiol devices. Since the device yield (~1.75%) of DC8 dithiol devices is not much different from that of C8 monothiol devices (~1.41%), this result may suggest that device yield is not much affected by metal–molecule contact, but rather affected more by the device structures, fabrication condition, and quality of the self-assembled monolayers. In this study, the use of a statistical approach is very significant, as the analysis of a large number of devices increases the ability to develop more accurate and meaningful characteristics of molecular systems. **Figures 10(a)–10(f)** present the statistical histograms of current densities in logarithmic scale for different lengths of alkanemonothiols (C8, C12, and C16) and alkanedithiols (DC8, DC9, and DC10) at 1.0 V with the mean positions as representative devices indicated with arrows from the fitting results by Gaussian functions. The current densities for these representative devices were found to be $\sim 8.3\times10^4$, 1.2×10^3, 3.5, 4.9×10^5, 2.0×10^5, and 6.3×10^4 A cm^{-2} at 1.0 V for C8, C12, C16, DC8, DC9, and DC10, respectively. The current densities–voltage ($\mathcal{J}$–V) characteristics for these six representative devices are plotted in **Figure 10(g)**. The conductance and $\mathcal{J}$–V characteristics are clearly dependent on the molecular length and metal–molecular contacts (i.e., monothiol vs. dithiol). This observation is supported by previous reports of M-M-M junctions that have shown that the current density for alkanedithiol is higher than that for alkanemonothiol due to their different natures of metal–molecule contact properties (chemisorbed vs. physisorbed contact) at Au–molecule contacts [64,65]. The histograms in **Figures 10(a)–10(f)** show the distribution of the logarithmic current densities, indicating the existence of fluctuation factors causing the exponential distribution in the current densities. The variation of junction area may exist, but the area fluctuation does not produce exponential distribution in current, instead fluctuation in the tunneling path is probably responsible for the distribution data of **Figures 10(a)–10(f)**. Some fluctuations in molecular configurations in the self-assembled monolayers in the device junctions are possible, such as fluctuations in molecular configuration or microstructures in metal–molecule contacts [66,67].

4.16.4.2.2 Contact/length-dependent decay coefficients by multibarrier tunneling model s0070

To investigate the effect of metal–molecule contacts p0200 on the electronic transport, we propose a multibarrier tunneling (MBT) model, which generalizes the Simmons tunneling model, a widely-used model for describing a rectangular tunneling barrier [9,10,57]. As compared to the Simmons tunneling model, where the tunneling barrier is represented by a single barrier, the M-M-M junction in MBT model can be divided into three parts: a molecular-chain body and metal–molecule contacts on either side of molecule, represented as three individual conduction barriers, as schematically illustrated in **Figure 11(a)**. In the

t0020 **Table 4** Summary of results for the fabricated devices

	Number of fabricated devices	*Fab. failure*	*Short*	*Open*	*Nonworking*	*Working*[a]			*Device yield*
						C8/DC8	*C12/DC9*	*C16/DC10*	
Monothiol	13,440 (100%)	392 (2.9%)	11,744 (87.4%)	1,103 (8.2%)	45 (0.3%)	63(1.41%)	33 (0.69%)	60 (1.44%)	156 (1.2%)
Dithiol	14,400 (100%)	472 (3.28%)	12.340 (85.7%)	1,252 (8.69%)	65 (0.45%)	84 (1.75%)	94 (1.96%)	93 (1.94%)	271 (1.9%)

[a] CS correspond to monothiol and DCs to dithiol.
Note: working and nonworking devices were defined by statistical analysis with Gaussian fitting on the histogram of the logarithmic scale current densities.

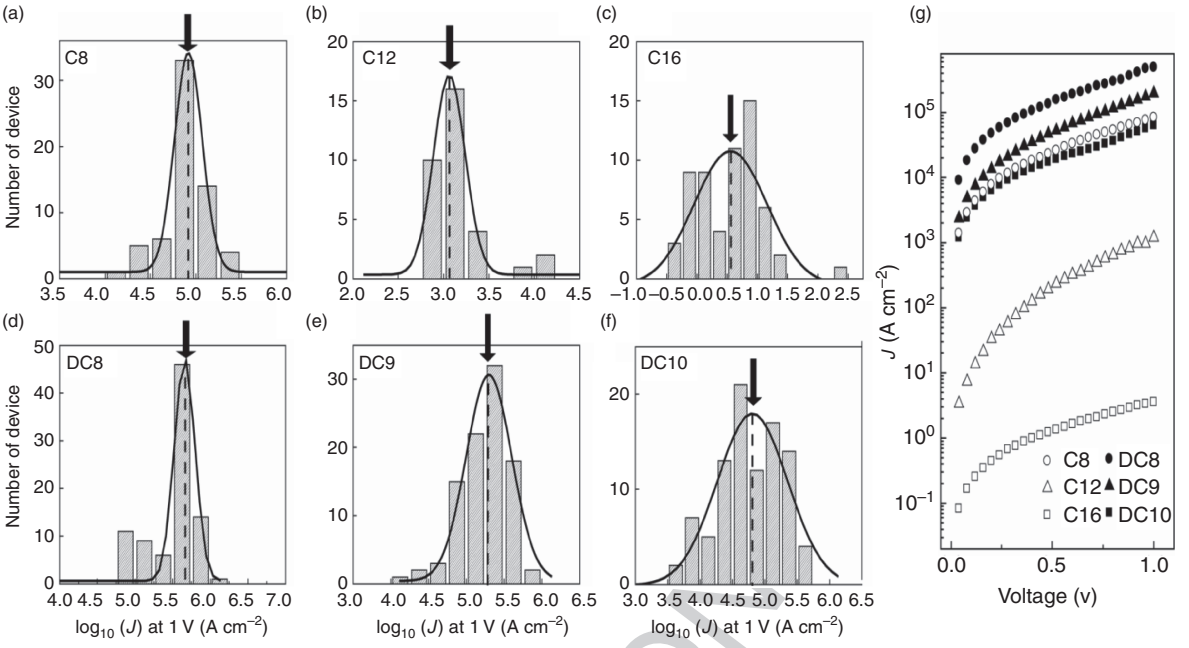

f0050 **Figure 10** The statistical histograms of log(*J*) measured at 1.0 V for C8 (a), C12 (b), C16 (c), DC8 (d), DC9 (e), and DC10 (f). The line curves are fitting results obtained from the histograms with Gaussian functions, and the mean positions are indicated with arrows. (g) Current density–voltage characteristics of representative devices chosen from the mean positions of the fitted Gaussian functions.

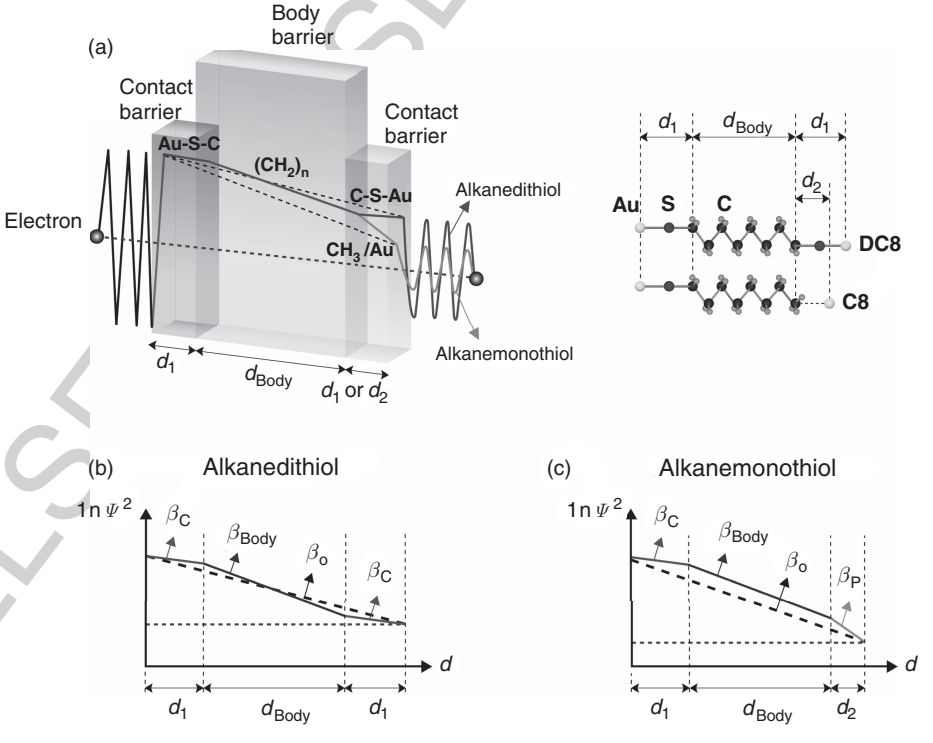

f0055 **Figure 11** (a) (Left) An illustration of MBT model; (Right) a schematic of barrier widths for C8 and DC8. Schematics of MBT model for an alkanedithiol M-M-M junction (b) and for an alkanemonothiol M-M-M junction (c).

alkanedithiol M-M-M junction, there is one molecular-chain body barrier [$(CH_2)_n$] (n is the number of carbon units), and two chemisorbed contact barriers [Au–S–C] on either side. Conversely, the alkanemonothiol M-M-M junction with the same a molecular-chain body barrier [$(CH_2)_n$] as the alkanedithiol junction has one chemisorbed contact barrier [Au–S–C] and one physisorbed contact barrier [CH_3/Au]. Please retain square brackets. This approach of separation of metal–molecule contact and molecular body from alkanethiol M-M-M junction is reasonable, since hybridization of the metal–molecule wave function decays rapidly into the junction for alkanethiol devices [68,69]. In the typical nonresonant tunneling case, the resistance is exponentially dependent on the molecular length $d(=d_1+ d_{1(2)} + d_{\mathrm{Body}})$. The widths of the barrier for d_1, d_{Body}, and d_2 in alkyl molecular system represent the length of the chemisorbed contact on the molecule [Au–S–C], the molecular body region [$(CH_2)_n$], and the physisorbed contact on the molecule [CH_3/Au], respectively. Here, we assume d_{Body} is the projected length along the molecular body with the incremental length per carbon atom ($\Delta d_{\mathrm{Body}}[CH_2]$) of ~1.25 Å and the contact lengths (d_1 and d_2) are the vertical distances between contact sites of molecule and electrode. The length d_{Body} is identical for n-alkanemonothiol and n-alkanedithiol with the same n value. For example, octanemonothiol (C8) and octanedithiol (DC8) have an identical length, $d_{\mathrm{Body}}[(CH_2)_8]$, ~8.75 Å. And, d_1 ([Au–S–C]) is ~3.2 Å and d_2([CH_3/Au]) is ~1.4 Å [70].

p0205 For small-length molecules with a large HOMO–LUMO energy gap, such as alkyl chain molecules, coherent tunneling is the main conduction mechanism of the electronic charge transport at relatively low bias regime [35]. As mentioned above, the tunneling current density in low-bias regime can be approximated as **equation 4a**. From **equation 4a**, β_o is the decay coefficient in a low-bias regime, which reflects the degree of decrease in wave function of the tunneling electron through the molecular tunnel barrier. A higher decay coefficient implies a faster decay of the wave function, that is, lower electron tunneling efficiency.

p0210 In MBT model, it is possible to describe the overall slope of wave function decay through the barriers based on the magnitude of the β_o value, and this overall decay can be further decomposed to three individual decays through three individual barriers, as shown in **Figure 11**. The β_o can be expressed as **equation 6** for alkanemonothiol (alkanedithiol) junctions from the consideration of geometric configurations.

$$\beta_o = \frac{\beta_C d_1 + \beta_{\mathrm{Body}} d_{\mathrm{Body}} + \beta_{C(P)} d_{1(2)}}{d_1 + d_{\mathrm{Body}} + d_{1(2)}} \quad (6)$$

One can see that β_o converges to β_{Body} for a very long molecule. Also, $\alpha(\Phi_B)^{1/2}$ can be expressed as **equation 7** by combining **equations 4a** and **6**:

$$\alpha(\Phi_B)^{1/2} = \frac{\hbar}{2(2m)^{1/2}} \frac{\beta_C d_1 + \beta_{\mathrm{Body}} d_{\mathrm{Body}} + \beta_{C(P)} d_{1(2)}}{d_1 + d_{\mathrm{Body}} + d_{1(2)}} \quad (7)$$

As mentioned above, because the main conduction mechanism is coherent (elastic) tunneling at low-bias regime (and at room temperature), it is assumed that the energy of electron tunneling through the molecular barriers does not decrease, as expressed by the horizontal dashed line in **Figure 11(a)**. Furthermore, due to the different nature of the metal–molecule contact properties, electron transmission for the chemisorbed contact [Au–S–C] is found to be more efficient than that for the physisorbed contact [CH_3/Au]. As a result, the slope (β_o) for alkanemonothiol junctions is steeper than that for alkanedithiol junctions, as illustrated by the dashed lines in **Figure 11**. In this MBT model, it was possible to define β_C (β_P) as the components of the decay coefficients corresponding to the chemisorbed (physisorbed) contact barrier width d_1 (d_2), as expressed by the solid lines in **Figure 11**. Similarly, β_{Body} is the decay coefficient component for the molecular-chain body barrier (center solid lines). p0215

Figure 12 shows the statistical distribution of β_o values obtained for different-length alkanemonothiol and alkanedithiol M-M-M devices. In this plot, β_o values were determined from fitting the I–V data of all the 'statistically defined working' molecular p0220

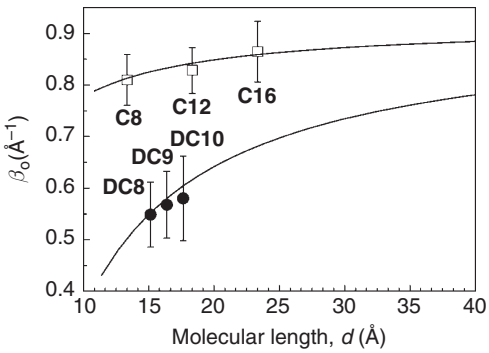

Figure 12 The mean (symbols) and standard deviations (error bars) of β_o versus molecular length d. The black solid lines were calculated from MBT model. f0060

electronic devices (total 427 devices) with the Simmons tunneling model. The values for the mean and standard deviation of β_o are presented as 0.81 ± 0.05, 0.83 ± 0.03, and 0.87 ± 0.05 Å^{-1} for C8, C12, and C16 alkanemonothiols, and 0.55 ± 0.06, 0.57 ± 0.06, and 0.58 ± 0.08 Å^{-1} for DC8, DC9, and DC10 alkanedithiols, respectively. As previously mentioned, the β_o values for alkanemonothiol devices appear to be larger than those for alkanedithiol devices due to the poor tunneling rate of physisorbed contact [CH_3/Au] in alkanemonothiol junctions, as compared to alkanedithiol junctions. Also, a slight increase of β_o values in **Figure 12** can be seen as the molecular length increases, which reflects the different tunneling rates for different lengths of alkanethiols, that is, the wave function of the tunneling electron decays further when it tunnels through longer molecules. The solid lines in **Figure 12** are the results calculated using the estimated β_{Body}, β_C, and β_P values determined from MBT model (**Table 5**). Moreover, **Figure 12** shows that the difference in β_o values between monothiol and dithiol becomes larger as the molecular length decreases. This phenomenon explains that the metal–molecular contact effect becomes relatively more important than the molecular-chain body effect in electronic transport for shorter molecules. On the contrary, if the molecular length increases, the molecular-chain body effect becomes more important and the β_o values of monothiol and dithiol molecular systems become closer and eventually converge to body decay coefficient (β_{Body}), as seen in **Figure 12**.

p0225 At low bias, **equations 3a** and **6** can be used to determine the resistance R of the ohmic regime as

$$R = \frac{4\pi^2\hbar^2}{A(2m)^{1/2}e^2}\left(\frac{d_1 + d_{Body} + d_{1(2)}}{(\Phi_B)^{1/2}\alpha}\right) \times \exp[\beta_1 d_1 + \beta_{Body} d_{Body} + \beta_{1(2)} d_{1(2)}] \quad (8)$$

where R_o is the contact resistance that can be defined in the limiting case when d_{Body} approaches zero, and expressed as **equation 9** for alkanemonothiol and alkanedithiol, respectively,

$$R_o = \frac{8\pi^2\hbar}{Ae^2}\left(\frac{(d_1 + d_{1(2)})^2}{\beta_1 d_1 + \beta_{1(2)} d_{1(2)}}\right)\exp[\beta_1 d_1 + \beta_{1(2)} d_{1(2)}] \quad (9)$$

Unlike the β_o value that describes the overall p0230 decay coefficient, the β_{Body} value is the decay coefficient component only for the molecular-chain body barrier. The molecular-chain body decay coefficient $\beta_{Body} = \Delta \ln R/\Delta d_{Body}$ can be determined from the slopes in the semilog plot of resistance R versus the molecular-chain body length d_{Body}, as shown in **Figure 13(a)**. Here, R is the resistance in the low-bias regime obtained from the linear fit of low-bias I–V data ($0 < V < 0.3$ V) for each device. From the slopes in **Figure 13(a)**, the β_{Body} values were determined to be $\sim 0.93 \pm 0.03$ and $\sim 0.92 \pm 0.08$ Å^{-1} for alkanemonothiol and alkanedithiol, respectively –almost identical values for the two molecular systems. Thus, one should note that the β_{Body} value is the molecular length-independent decay coefficient that is dependent upon molecular structure but not on metal–molecule contacts, whereas the β_o value is the molecular length-dependent overall decay coefficient that depends not only on the molecular structures but also on the form of metal–molecule contact (i.e., chemisorbed or physisorbed). The β_C, β_P, and β_o for the alkyl M-M-M junctions can be calculated from the observed $\beta_{Body} \sim 0.92$ Å^{-1}, β_o values for C8 and DC8, and the widths of barriers (d_1, d_{Body}, and d_2). The contact resistance (R_o) can be considered a method of investigating the metal–molecule contacts. However, since R_o depends on the junction area, the specific contact resistance (R_C) (a junction-area-compensated quantity) is generally obtained and compared among devices with different junction areas. **Figure 13(b)** presents the

t0025 **Table 5** A summary of the experimental and calculated values for decay coefficients, contact resistances, and specific contact resistances

	β_{Body} (Å^{-1})	β_1(Å^{-1})	β_2(Å^{-1})	R_0(Ω)	R_c(Ω cm^2)
Alkanemonothiol					
Calculated value	0.92	0.05	1.89	0.19	0.58×10^{-8}
Experimental value	0.93 ± 0.03			0.34 ± 0.30	$1.08 \pm 0.94 \times 10^{-8}$
Alkanedithiol					
Calculated value	0.92	0.05		0.03	0.98×10^{-9}
Experimental value	0.92 ± 0.08			0.04 ± 0.03	$1.13 \pm 0.98 \times 10^{-9}$

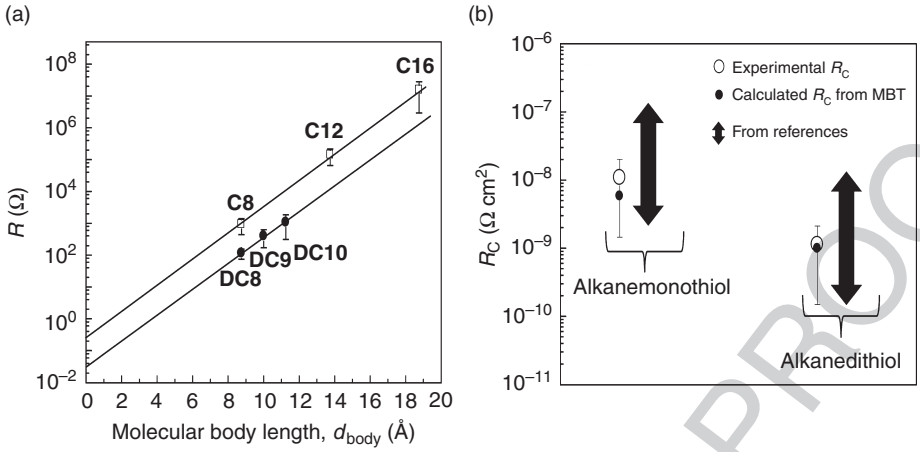

f0065 **Figure 13** (a) Semilog plot of the resistance R versus the molecular-chain body length d_{Body} for alkanemonothiol and alkanedithiol junctions. The solid lines are exponential fitting results, giving the molecular-chain body decay coefficient β_{Body}. (b) Experimental and calculated specific contact resistance R_C. The blue arrows represent the range of the estimated R_C values from the contact resistances reported in literature [24,64,71a,b].

experimental and theoretical values for R_C for our alkanemonothiol and alkanedithiol devices at a low-bias regime. Here, the specific contact resistance $R_C(=R_o \times A)$ can be obtained by multiplying the contact resistance (R_o) with the contact junction area (A) ($\sim 3.14 \times 10^{-8}$ cm^2 for our molecular devices). The contact resistance (R_o) was found by extrapolating the observed resistance (**Figure 13(a)**) to a zero molecular-chain body length ($\sim 0.34 \pm 0.3\ \Omega$ for alkanemonothiol, and $\sim 0.04 \pm 0.03\ \Omega$ for alkanedithiol). Then, R_C was calculated as $(\sim 1.08 \pm 0.94) \times 10^{-8}\ \Omega$ cm^2 for alkanemonothiol and $(\sim 1.13 \pm 0.98) \times 10^{-9}\ \Omega$ cm^2 for alkanedithiol. Using MBT model, R_C could also be estimated as $\sim 0.58 \times 10^{-8}\ \Omega$ cm^2 for alkanemonothiol and $\sim 0.98 \times 10^{-9}\ \Omega$ cm^2 for alkanedithiol, both of which are in good agreement with the experimental values we obtained. **Table 5** summarizes the experimental and calculated quantities of decay coefficients and contact and specific contact resistances for our measurements.

p0235 Note that our analysis with MBT model does not consider the details of the Fermi level alignment and molecular binding sites, which will generally influence the charge transport of molecular devices. Furthermore, the transport properties values obtained from our experimental results with microscale molecular junctions are an ensemble average effect with various microstructures of metal–molecule contacts and binding sites, and thus should not be compared with single-molecular measurement results, due to the contribution from the probability amplitude of multiple reflections and the possibility of cooperative effects between individual molecules in ensemble of molecules.

4.16.4.2.3 Contact properties through various electrodes by multi–barrier tunneling model s0075

Similarly, using **equation 4a**, the contact decay coefficients $\beta_{C(P)}$ for Au contacts can be expressed as p0240

$$\beta_{C(P)} = \frac{2(2m)^{1/2}}{\hbar} \alpha_{C(P)} (\Phi_{C(P)})^{1/2} \qquad (10)$$

where $\Phi_{C(P)}$ is the contact barrier height at zero bias and $\alpha_{C(P)}$ the α value through the contact barrier. These two value can be obtained from α and Φ_B in Au–alkyl molecule contacts, which can be deduced from the molecular body decay coefficients (β_{Body}) and widths (d_1, d_2, and d_{Body}) of each barrier part.

Furthermore, the decay coefficients and specific contact resistance can be determined for molecular junctions with various metal contacts other than Au. If molecular monolayers are sandwiched between other metals (Ag and Cu), the contact barrier heights can be expressed as $\Phi_{C(other\ metals)} = \Phi_{C(Au)} + \Delta\Phi_{(Au-other\ metals)}$ and $\Phi_{P(other\ metals)} = \Phi_{P(Au)} + \Delta\Phi_{(Au-other\ metals)}$ for chemisorbed contact and physisorbed contact, respectively, by assuming the tunneling around HOMO levels (i.e., a hole type tunneling). Note that $\Delta\Phi_{(Au-other\ metals)}$ is the difference between the work function of Au and that of the other metal. From **equation 10** with using Φ_C, Φ_P, α_C, and α_P, the contact decay coefficient $\beta_{C(P)(Ag\ and\ Cu)}$ can be calculated as ($\beta_{C(Ag)} = 0.51$ Å^{-1} and p0245

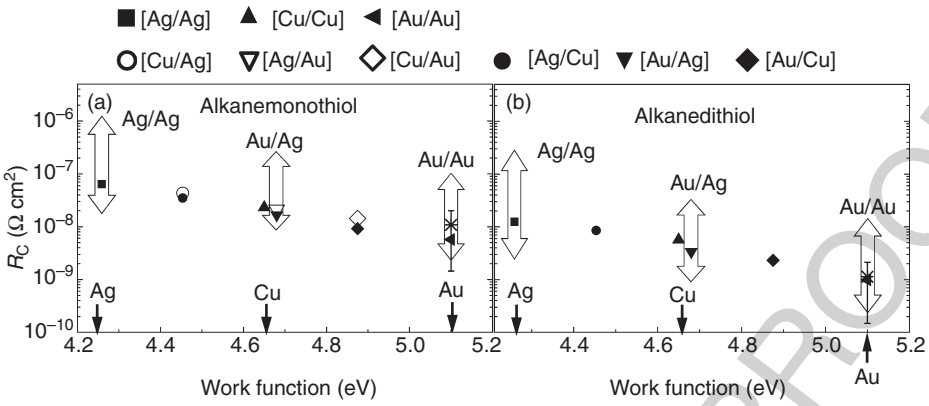

f0070 **Figure 14** The specific contact resistance R_C for (a) alkanemonothiol and (b) alkanedithiol obtained from the MBT model as a function of metal work function. Open arrows are a range of R_C values estimated from literature [24,64,71a,b]. The black crosses for [Au/Au] are the experimental values obtained in our study.

$\beta_{C(Cu)} = 0.38$ Å^{-1}) and ($\beta_{P(Ag)} = 2.76$ Å^{-1} and $\beta_{P(Cu)} = 2.28$ Å^{-1}) for chemisorbed contacts and physisorbed contacts, respectively.

p0250 **Figure 14** shows the R_C values of various metal–molecule contacts (Ag, Cu, and Au) in alkyl M-M-M junctions obtained from experiment, reported studies, and the MBT model, by assuming tunneling around HOMO, that is, a hole type tunneling. In this **Figure 7**, the labels are designed such that, for example, [Au/Ag] refers to [Au–S–$(CH_2)_{n-1}CH_3$/Ag], that is, the chemisorbed contact to the Au electrode and physisorbed contact to the Ag electrode for alkanemonothiol (**Figure 14(a)**) or [Au–S–$(CH_2)_n$–S–Ag], that is, the chemisorbed contacts to both Au and Ag electrodes for alkanedithiol (**Figure 14(b)**). And for different metallic junctions (e.g., [Au/Ag], [Ag/Cu], etc.), the average value of the two individual metal work functions was assigned as the work function. As mentioned earlier, the natures of the chemisorbed and physisorbed contacts are quite different. Because the chemisorbed contacts ([metal–S–C]) can form stronger bondings by molecular overlapping than physisorbed contacts (metal/CH_3 or metal/H), generally the contact decay coefficient for chemisorbed contacts are smaller than that of physisorbed contacts ($\beta_C < \beta_P$), that is, less tunneling electron decay through chemisorbed contacts. In MBT model, the contact decay coefficients (β_C, β_P) in various metallic junctions are dependent on the contact barrier height (Φ_C, Φ_P) and effective mass (α_C and α_P), which can be affected by metal work function, as expressed in **equation 10**. Note that the contact decay coefficient was observed to decrease when metal work function is increased. The R_C values were found to be different for asymmetric metal contacts (e.g., [Ag/Au] and [Au/Ag]) for alkanemonothiol because of the different natures of metal–molecule contacts (physisorbed vs. chemisorbed contact side), as shown in **Figure 14(a)**, whereas R_c values for that of alkanedithiol were found to be same for even asymmetric contacts because of the same nature of metal–molecule contact, as shown in **Figure 14(b)**. As a result, it was determined that when the average metal work function increases, R_C decreases due to a reduction of the contact barrier height (or contact decay coefficients). The R_C values calculated by the MBT model are in good agreement with those obtained from reported literatures [24,64,71a,b], as indicated by the arrows, as shown in **Figure 14**.

4.16.4.3 Inelastic Tunneling s0080

4.16.4.3.1 Inelastic electron tunneling spectroscopy s0085

p0255 Electronic transport through alkanethiol SAMs is further investigated with the technique of inelastic electron tunneling spectroscopy [36], for example, by Jaklevic and Lambe, who studied, in 1966, the conductance of tunnel junctions with encased organic molecules [37]. Since then it has become a powerful spectroscopic tool for chemical identification, chemical bonding investigation, and studies in surface chemistry and physics [40]. In an inelastic tunneling process, the electron loses energy to a localized vibrational mode with a frequency ν when the applied bias satisfies the condition of $eV = h\nu$. As a result, an additional tunneling channel is opened for

the electron, resulting in an increase in the total current at the applied bias corresponding to the vibrational mode energy [39]. Typically only a small fraction of tunneling electrons are involved in the inelastic tunneling process (determined by the electron–vibronic mode coupling coefficient), resulting in a small conductance change, which is commonly measured in the second harmonics of a phase-sensitive detector that yields the characteristic frequencies of the corresponding vibrational modes as well as other information [38–40].

p0260 Measurements of $I(V,T)$ and additional IETS studies have been performed on an octanedithiol (C8-dithiol) SAM using the aforementioned device structure shown in **Figure 1(a)** [36]. **Figure 15(a)** is the $I(V,T)$ data for this device obtained from 300 to 4.2 K. An Arrhenius plot shown in **Figure 15(b)** exhibits mild temperature dependence, verifying that tunneling is the main transport mechanism for C8-dithiol SAM. This result is in good agreement with the tunneling transport characteristics observed previously. **Figure 15(c)** shows the room temperature $I(V)$ measurement result. Using a junction area of 51 ± 5 nm in diameter (obtained from statistical studies of the nanopore size with SEM), a current density of $(9.3 \pm 1.8)\times 10^{-4}$ A cm^{-2} at 1.0 V is calculated. As a comparison, the current density of $(3.1 \pm 1.0)\times 10^{4}$ A cm^{-2} at 1.0 V was observed for C8 monothiol SAM. Using the modified Simmons model (**equation 2**), the transport parameters of $\Phi_B = 1.20 \pm 0.03$ eV and $\alpha = 0.59 \pm 0.01$ ($m^* = 0.34m$) were obtained for this C8-dithiol SAM.

p0265 **Figure 16** shows the IETS spectrum of the same C8-dithiol SAM device obtained at $T = 4.2$ K. An AC modulation of 8.7 mV (root-mean-square (RMS) value) at a frequency of 503 Hz was applied to the sample to acquire the second-harmonic signals. The spectra are stable and repeatable upon successive bias sweeps. The spectrum at 4.2 K is characterized by three pronounced peaks in the 0–200 mV region at 33, 133, and 158 mV. From a comparison with previously reported infrared (IR), Raman, and high-resolution electron energy loss (HREEL) spectra of SAM covered gold surfaces (**Table 6**), these three peaks are assigned to ν(Au–S), ν(C–C), and $\gamma_w(CH_2)$ modes of a surface bound alkanethiolate [72–75]. The absence of a strong ν(S–H) signal at ~329 mV suggests that most of the thiol groups have reacted with the gold bottom and top contacts. Peaks are also reproducibly observed at 80, 107, and 186 mV. They correspond to ν(C–S), $\delta_r(CH_2)$, and $\delta_s(CH_2)$ modes. The stretching mode of the CH_2 groups, $\nu(CH_2)$, appears as a shoulder at 357 meV. The peak at 15 mV is due to vibrations from either Si, Au, or δ(C–C–C) [76]. We note that all alkanethiolate peaks without exception or omission occur in the spectra. Peaks at 58, 257, 277, and 302 mV, as well as above 375 mV are likely to originate from Si–H and N–H vibrations related to the silicon nitride membrane [76a,77a,b], which forms the SAM encasement. To the best of our knowledge, alkanethiols have no vibrational signatures in these regions. Measurement of the background spectrum of an 'empty' nanopore device with only gold contacts to obtain background contributions from Si_3N_4 is hampered by either too low (open circuit) or too high (short circuit) currents in such a device. Similar IETS result has also been obtained using a different test structure recently [78].

p0270 Although there are no selection rules in IETS as there are in IR and Raman spectroscopy, certain selection preferences have been established. According to the IETS theory [79], molecular vibrations with net dipole moments perpendicular to the interface of the tunneling junction have stronger peak intensities than vibrations with net dipole moments parallel to the interface (for dipoles close to the electrodes). Thus, vibrations perpendicular to the electrode interface, that is, ν(Au–S), ν(C–S), ν(C–C), and $\gamma_w(CH_2)$, dominate the IETS spectrum, while modes parallel to the interface, that is, $\delta_{r,s}(CH_2)$ and $\nu(CH_2)$, are weak, as clearly shown in **Figure 16**.

4.16.4.3.2 Linewidth study s0090

p0275 In order to verify that the observed spectra are indeed valid IETS data, the peak width broadening was examined as a function of temperature and modulation voltage. IETS was performed with different AC modulations at a fixed temperature, and at different temperatures with a fixed AC modulation. **Figure 17(a)** shows the modulation dependence of the IETS spectra obtained at 4.2 K, and **Figure 17(b)** shows the modulation broadening of the C–C stretching mode at 133 meV. The circular symbols are the full widths at half maximum (FWHMs) of the experimental peak at $T = 4.2$ K with various modulation voltages. A Gaussian distribution function was utilized to obtain an FWHM and the error range [80]. The square symbols are calculated FWHM values ($W_{theoretical}$) taking into account both a finite-temperature effect ($W_{thermal} \sim 5.4\,k_BT$)[38] and a finite-voltage modulation effect ($W_{modulation} \sim 1.7\,V_{ac\_RMS}$) [81]. These two broadening contributions add as the squares: $W^2_{theoretical} = W^2_{thermal} +$

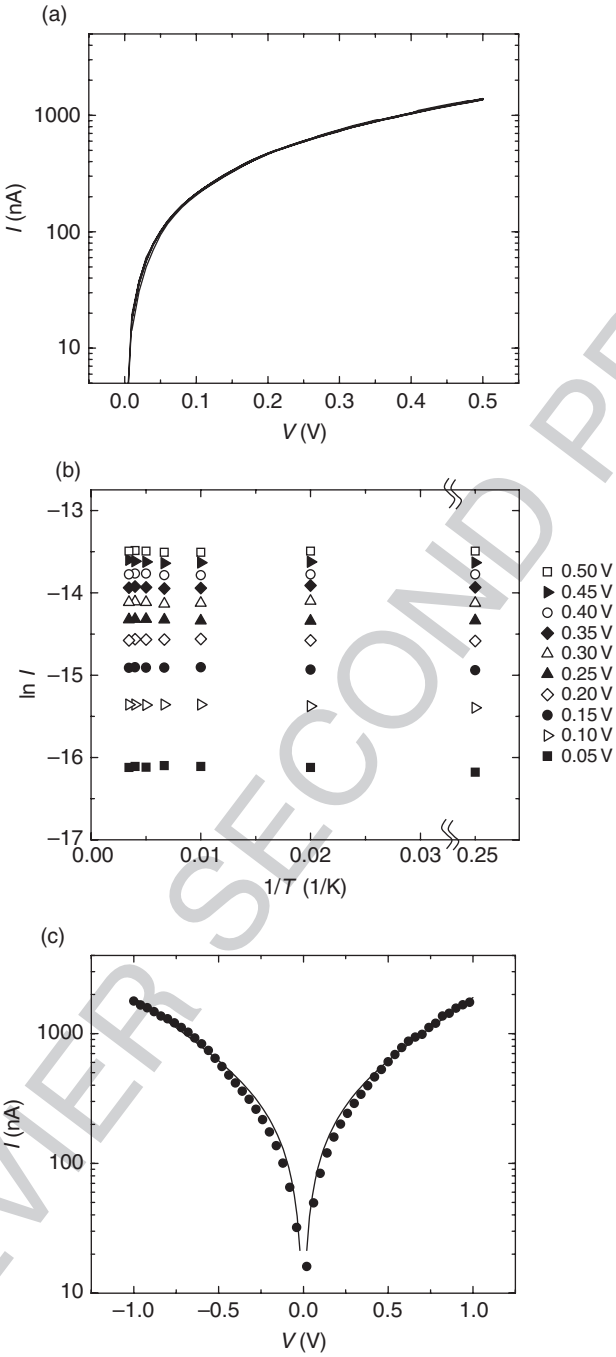

f0075 **Figure 15** (a) $I(V,T)$ characteristics of C8 dithiol SAM at selected temperatures (4.2, 50, 100, 150, 200, 250, and 290 K). (b) Arrhenius plot generated from the data in (a), at voltages from 0.1 to 0.5 V with 0.05 V steps. (c) Measured C8-dithiol $I(V)$ data at room temperature (circular symbols) is compared with calculation (solid curve) using the optimum fitting parameters of $\Phi_B = 1.20$ eV and $\alpha = 0.59$.

$W^2_{\text{modulation}}$. The agreement is excellent over most of the modulation range, but we note a saturation of the linewidth at low-modulation bias indicating the influence of a non-negligible intrinsic linewidth. Taking into account the known thermal and modulation broadenings, and including the intrinsic linewidth (W_I) [82] as a fitting parameter, the measured peak width (W_{exp}) is given by

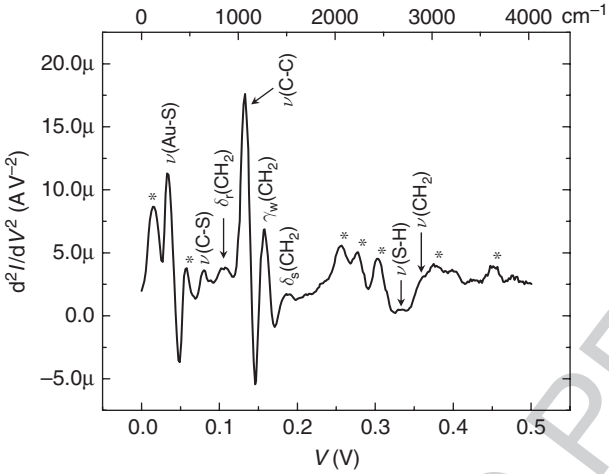

f0080 **Figure 16** Inelastic electron tunneling spectrum of C8 dithiol SAM obtained from lock-in second-harmonic measurement with an AC modulation of 8.7 mV (RMS value) at a frequency of 503 Hz ($T = 4.2$ K). Peaks labeled * are most probably background due to the encasing Si_3N_4.

t0030 **Table 6** Summary of the major vibrational modes of alkanethiolates

Modes	*Methods*	*Wavenumber (cm^{-1})*	*(meV)*
ν(Au–S)	HREELS [61]	225	28
ν(C–S)	Raman [60a,b]	641	79
	Raman [60a,b]	706	88
$\delta_r(CH_2)$	HREEL [61]	715	89
	IR [62]	720	89
	IR [62]	766	95
	IR [62]	925	115
ν(C–C)	HREEL [61]	1050	130
	Raman [60a,b]	1064	132
	Raman [60a,b]	1120	139
	IR [62]	1230	152
	HREELS [61]	1265	157
	IR [62]	1283	159
	IR [62]	1330	165
$\delta_s(CH_2)$	HREELS [61]	1455	180
ν(S–H)	Raman [60a,b]	2575	319
$\nu_s(CH_2)$	Raman [60a,b]	2854	354
	HREELS [61]	2860	355
$\nu_{as}(CH_2)$	Raman [60a,b]	2880	357
	Raman [60a,b]	2907	360
	HREELS [61]	2925	363

Note: There is a vast amount of literature with spectroscopic assignments for alkanethiols. The references given are representative for IR, Raman, and HREELS assignments. From Bryant MA and Pemberton JE (1991) *Journal of the American Chemical Society* 113: 8284; Kato HS, Noh J, Hara M, and Kawai M (2002) *Journal of Physical Chemistry B* 106: 9655; Castiglioni C, Gussoni M, and Zerbi GJ (1991) *Chemical Physics* 95: 7144.

$$W_{\text{exp}} = \sqrt{W_I^2 + W_{\text{thermal}}^2 + W_{\text{modulation}}^2} \qquad (11)$$

W_I can be determined by using a nonlinear least-squares fit to the AC modulation data (**Figure 17**) with **equation 11**, giving an intrinsic linewidth of 3.73 ± 0.98 meV for this line. This is shown (with the error range) in **Figure 17(b)** as a shaded bar, including the thermal contribution.

We can independently check the thermal broadening of the line at fixed modulation. **Figure 18(a)** shows the temperature dependence of the IETS spectra obtained with an AC modulation of 8.7 mV (RMS value). In **Figure 18(b)** the circular symbols (and corresponding error bars) are experimental FWHM values of the C–C stretching mode from **Figure 18(a)**, determined by a Gaussian fit (and error of the fit) to the experimental lineshape. For simplicity, we have considered only Gaussian lineshapes [80], resulting in increased error bars for the lower-temperature range due to an asymmetric lineshape. The square symbols are theoretical calculations considering thermal broadening, modulation broadening, and the intrinsic linewidth determined above. The error ranges of the calculation (due to the intrinsic linewidth error) are approximately the size of the data points. The agreement between theory and experiment is very good, spanning a temperature range from below ($\times 0.5$) to above ($\times 10$) the thermally broadened intrinsic linewidth. This linewidth should be a sensitive test to compare to theoretical models of transmission probabilities [83]. p0280

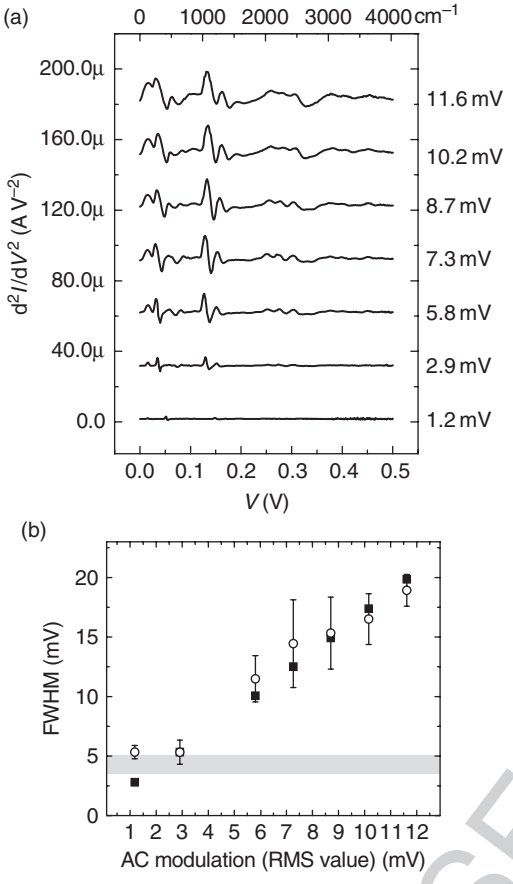

f0085 **Figure 17** (a) Modulation dependence of IETS spectra obtained at 4.2 K. (b) Line (C–C stretching mode) broadening as a function of AC modulation. The circular symbols are experimental FWHMs and the square symbols are theoretical calculations considering both modulation and thermal contributions. The shaded bar denotes the expected saturation due to the derived intrinsic linewidth (including a $5.4k_BT$ thermal contribution) of 3.73 ± 0.98 meV.

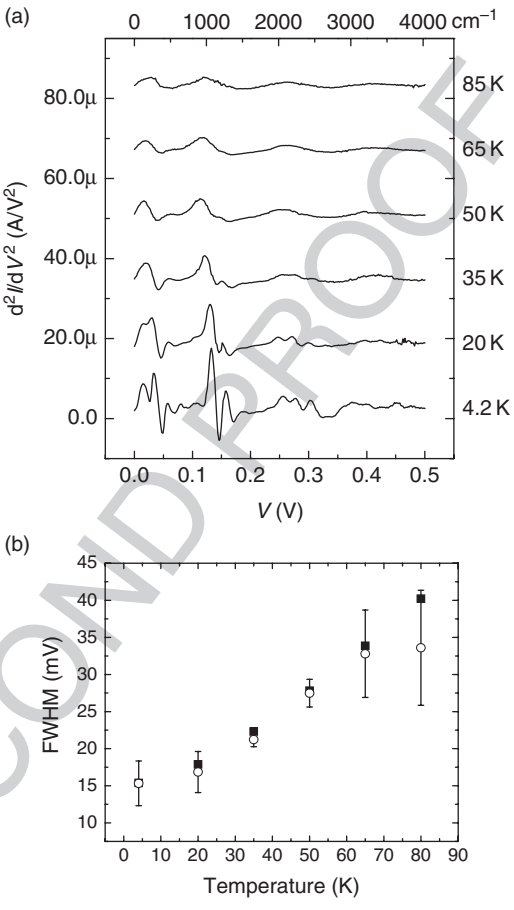

Figure 18 (a) Temperature dependence of IETS spectra obtained at a fixed AC modulation of 8.7 mV (RMS value). (b) Line (C–C stretching mode) broadening as a function of temperature. The circular symbols are experimental FWHMs and the square symbols are theoretical calculations considering thermal broadening, modulation broadening, and the intrinsic linewidth. f0090

s0095 4.16.5 Conclusions

p0285 We present here a study of electronic transport properties of alkanethiol SAMs, with the intent that this system can serve as a simple standard for the development of well-characterized molecular junctions. The characteristics are consistent with accepted models of tunneling junctions, as well as presenting a system on which tunneling spectroscopy can be performed. The metal–molecule contact plays a crucial role in the charge transport through the molecular junctions.

p0290 The field of 'molecular electronics' is rich in the proposal and promise of numerous device concepts [84,85], but unfortunately reliable data and characterization techniques upon which to test these ideas are not available. It is incumbent upon the experimentalists to carefully institute controls to validate claims of intrinsic molecular behavior. Systematic controls, such as the model system presented here, should assist in guiding further work toward a rational development of the fascinating device structures and systems that the field promises.

Acknowledgments

This work was supported by DARPA/ONR (N00014-01-1-0657), ARO (DAAD19-01-1-0592), AFOSR (F49620-01-1-0358), NSF (DMR-0095215),

and NASA (NCC 2-1363). Authors (G.W., T.-W. K., and T. L.) thank financial supports from the National Research Laboratory (NRL) Program of the Korea Science and Engineering Foundation (KOSEF), the Program for Integrated Molecular System at Gwangju Institute of Science and Technology.

References

b0005 1. Reed MA and Lee T (2003) *Molecular Nanoelectronics*. Stevenson Ranch, CA: American Scientific Publishers.

b0010 2a. Aviram A and Ratner MA (1974) Molecular rectifier. *Chemical Physics Letters* 29: 277.

b0015 2b. Chen J, Reed MA, Rawlett AM, and Tour JM (1999) Electron transport in molecular wire junctions. *Science* 286: 1550.

b0020 3a. Chen J, Reed MA, Rawlett AM, and Tour JM (1999) Large on-off ratios and negative differential resistance in a molecular electronic device. *Science* 286: 1550.

b0025 3b. Chen Y, Jung G-Y, Ohlberg DAA, *et al.* (2003) Nanoscale molecular-switch crossbar circuits. *Nanotechnology* 14: 462.

b0030 3c. Stewart DR, Ohlberg DAA, Beck PA, *et al.* (2004) Molecule-independent electrical switching in Pt/organic monolayer/Ti devices. *Nano Letters* 4: 133.

b0035 3d. Green JE, Choi JW, Boukai A, *et al.* (2007) A 160,000 bit molecular electronic memory circuit patterned at 1011 bits per square centimeter. *Nature* 445: 414.

b0040 4a. Selzer Y, Salomon A, and Cahen D (2002) The importance of chemical bonding to the contact for tunneling through alkyl chains. *Journal of Physical Chemistry B* 106: 10432.

b0045 4b. Guisinger NP, Greene ME, Basu R, Baluch AS, and Hersam MC (2004) Room temperature negative differential resistance through individual molecules on silicon surfaces. *Nano Letters* 4: 55.

b0050 4c. Xiao X, Xu B, and Tao NJ (2004) Measurement of single molecule conductance: Benzenedithiol and benzenedimethanethiol. *Nano Letters* 4: 267.

b0055 4d. Donhauser ZJ, Mantooth BA, Kelly KF, *et al.* (2001) Conductance switching in single molecules through conformational changes. *Science* 292: 2303.

b0060 4e. Ramachandran GK, Hopson TJ, Rawlett AM, Nagahara LA, Primak A, and Lindsay SM (2003) A bond-fluctuation mechanism for stochastic switching in wired molecule. *Science* 300: 1413.

b0065 5. Hewlett-Packard Quantum Science Research, Beyond Silicon: Breakthroughs in Molecular Electronics. http://www.hpl.hp.com/research/qsr/ (accessed September 2009).

b0070 6a. Luo Y, Collier CP, Jeppesen JO, *et al.* (2002) Two-dimensional molecular electronics circuits. *ChemPhysChem* 3: 519.

b0075 6b. Collier CP, Mattersteig G, and Wong EW, *et al*. (2000) A [2]catenane-based solid state electronically reconfigurable switch. *Science*. 289: 1172.

b0080 7. Lau CN, Stewart DR, Williams RS, and Bockrath M (2004) Direct observation of nanoscale switching centers in metal/molecule/metal structures. *Nano Letters* 4: 569.

b0085 8. Lee T, Wang W, Klemic JF, Zhang JJ, Su J, and Reed MA (2004) Comparison of electronic transport characterization methods for alkanethiol self-assembled monolayers. *Journal of Physical Chemistry B* 108: 8742.

b0090 9. Wang G, Kim T-W, Lee H, and Lee T (2007) Influence of metal-molecule contacts on decay coefficients and specific contact resistances in molecular junctions. *Physical Review B* 76: 205320.

10. Wang G, Kim T-W, Jang YH, and Lee T (2008) Effects of metal-molecule contact and molecular structure on molecular electronic conduction in nonresonant tunneling regime: Alkyl versus conjugated molecules. *Journal of Physical Chemistry C* 112: 13010. b0095

11. Ulman A (1991) *An Introduction to Ultrathin Organic Filmsfrom Langmuir–Blodgett to Self-Assembly*. Boston, MA: Academic Press. b0100

12. Poirier GE (1997) Characterization of organosulfur molecular monolayers on Au(111) using scanning-tunneling-microscopy. *Chemical Reviews* 97: 1117. b0105

13. Ratner MA, Davis B, Kemp M, Mujica V, Roitberg A, and Yaliraki S (1998) In: Aviram A and Ratner M (eds.) *Molecular Electronics: Science and Technology, the Annals of the New York Academy of Sciences*, vol. 852. New York: New York Academy of Sciences. b0110

14. Although the HOMO–NUMO gap of alkyl chain type molecules has been reported (see Ref. 15), there is no experimental data on the HOMO–LUMO gap for Au/alkanethiol SAM/Au system. 8 eV is commonly used as HOMO–LUMO gap of alkanethiol. b0115

15a. Boulas C, Davidovits JV, Rondelez F, and Vuillaume D (1996) Suppression of charge carrier tunneling through organic self-assembled monolayers. *Physical Review Letters* 76: 4797. b0120

15b. Fujihira M and Inokuchi H (1972) Photoemission from polyethylene. *Chemical Physics Letters* 17: 554. b0125

15c. Lias SG, Bartmess JE, Liebman JF, Holmes JL, Levin RD, and Mallard WG (1998) Gas-phase ion and neutral thermochemistry. *Journal of Physical and Chemistry Reference Data* 17(1): 24. b0130

15d. Yang H-H and McCreery RL (1999) Electron-transfer kinetics and adsorption of methyl viologen and phenothiazine derivatives on glassy carbon electrodes. *Analytical Chemistry* 71: 4081. b0135

16. Walczak MW, Chung C, Stole SM, Widrig CA, and Porter MD (1991) Effects of surface monolayers on the el, Structure and interfacial properties of spontaneously adsorbed *n*-alkanethiolate monolayers on evaporated silver surfaces. *Journal of the American Chemical Society* 113: 2370. b0140

17. Nuzzo RG, Zegarski BR, and Dubois LH (1987) Fundamental studies of the chemisorption of organosulfur compounds on gold(111). Implications for molecular self-assembly on gold surfaces. *Journal of the American Chemical Society* 109: 733. b0145

18. Widrig CA, Chung C, and Porter MD (1991) The electrochemical desorption of *n*-alkanethiol monolayers from polycrystalline Au and Ag electrodes. *Journal of Electroanalytical Chemistry* 310: 335. b0150

19. Poirier GE and Tarlov MJ (1994) The $c(4\times2)$ superlattice of alkanethiol self-assembled monolayers on Au(111). *Langmuir* 10: 2853. b0155

20. Porter MD, Bright TB, Allara DL, and Chidsey CED (1987) Spontaneously organized molecular assemblies. 4. Structural characterization of *n*-alkyl thiol monolayers on gold by optical ellipsometry, infrared spectroscopy, and electrochemistry. *Journal of the American Chemical Society* 109: 3559. b0160

21. Bumm LA, Arnold JJ, Dunbar TD, Allara DL, and Weiss PS (1999) Electron tunneling through organic molecules. *Journal of Physical Chemistry B* 103: 8122. b0165

22. Xu B and Tao NJ (2003) Measurement of single-molecule resistance by repeated formation of molecular junctions. *Science* 301: 1221. b0170

23. Wold DJ and Frisbie CD (2001) Fabrication and characterization of metal–molecule–metal junctions by conducting probe atomic force microscopy. *Journal of the American Chemical Society* 123: 5549. b0175

b0180 24. Wold DJ, Haag R, Rampi MA, and Frisbie CD (2002) Distance dependence of electron tunneling through self-assembled monolayers measured by conducting probe atomic force microscopy: Unsaturated versus saturated molecular junctions. *Journal of Physical Chemistry B* 106: 2813.

b0185 25. Cui XD, Zarate X, Tomfohr J, *et al*. (2002) Making electrical contacts to molecular monolayers. *Nanotechnology* 13: 5.

b0190 26. Cui XD, Primak A, Zarate X, *et al*. (2002) Changes in the electronic properties of a molecule when it is wired into a circuit. *Journal of Physical Chemistry B* 106: 8609.

b0195 27. Holmlin R, Haag R, Chabinyc ML, *et al*. (2001) Electron transport through thin organic films in metal–insulator–metal junctions based on self-assembled monolayers. *Journal of the American Chemical Society* 123: 5075.

b0200 28. Rampi MA and Whitesides GM (2002) A versatile experimental approach for understanding electron transport through organic materials. *Chemical Physics* 281: 373.

b0205 29. Slowinski K, Fong HKY, and Majda M (1999) Mercury–mercury tunneling junctions. 1. Electron tunneling across symmetric and asymmetric alkanethiolate bilayers. *Journal of the American Chemical Society* 121: 7257.

b0210 30. York RL, Nguyen PT, and Slowinski K (2003) Long-range electron transfer through monolayers and bilayers of alkanethiols in electrochemically controlled Hg–Hg tunneling junctions. *Journal of the American Chemical Society* 125: 5948.

b0215 31. Kushmerick JG, Holt DB, Pollack SK, *et al*. (2002) Effect of bond-length alternation in molecular wires. *Journal of the American Chemical Society* 124: 10654.

b0220 32. Smalley JF, Feldberg SW, Chidsey CED, Linford MR, Newton MD, and Liu Y (1995) The kinetics of electron transfer through ferrocene-terminated alkanethiol monolayers on gold. *Journal of Physical Chemistry* 99: 13141.

b0225 33. Weber K, Hockett L, and Creager S (1997) Long-range electronic coupling between ferrocene and gold in alkanethiolate-based monolayers on electrodes. *Journal of Physical Chemistry B* 101: 8286.

b0230 34. Slowinski K, Chamberlain RV, Miller CJ, and Majda M (1997) Through-bond and chain-to-chain coupling. Two pathways in electron tunneling through liquid alkanethiol monolayers on mercury electrodes. *Journal of the American Chemical Society* 119: 11910.

b0235 35. Wang W, Lee T, and Reed MA (2003) Electron conduction mechanism in self-assembled alkanethiol monolayer devices. *Physical Review B* 68: 035416.

b0240 36. Wang W, Lee T, Kretzschmar I, and Reed MA (2004) Inelastic electron tunneling spectroscopy of alkanedithiol self-assembled monolayers. *Nano Letters* 4: 643.

b0245 37. Jaklevic RC and Lambe J (1966) Molecular vibration spectra by electron tunneling. *Physical Review Letters* 17: 1139.

b0250 38. Lambe J and Jaklevic RC (1968) Molecular vibration spectra by inelastic electron tunneling. *Physical Review* 165: 821.

b0255 39. Adkins CJ and Phillips WA (1985) Inelastic electron tunnelling spectroscopy. *Journal of Physics C: Solid State Physics* 18: 1313.

b0260 40. Hansma PK (ed.) (1982) *Tunneling Spectroscopy: Capabilities, Applications, and New Techniques*. New York: Plenum.

b0265 41. Stipe BC, Rezaei MA, and Ho W (1998) Single-molecule vibrational spectroscopy and microscopy. *Science* 280: 1732.

b0270 42. Zhou C, Deshpande MR, Reed MA, Jones L, II, and Tour JM (1997) Nanoscale metal/self-assembled monolayer/metal heterostructures. *Applied Physics Letters* 71: 611.

b0275 43. Chen J, Calvet LC, ReedMA, Carr DW, Grubisha DS, and Bennett DW (1999) Electronic transport through metal–1,4-phenylene diisocyanide–metal junctions. *Chemical Physics Letters* 313: 741.

b0280 44. Ralls KS, Buhrman RA, and Tiberio RC (1989) Fabrication of thin-film metal nanobridges. *Applied Physics Letters* 55: 2459.

b0285 45. Kim T-W, Wang G, Lee H, and Lee T (2007) Statistical analysis of electronic properties of alkanethiols in metal–molecule–metal junctions. *Nanotechnology* 18: 315204.

b0290 46. Ethanol and alkane molecules were purchased from Sigma-Aldrich

b0295 47. Metzger RM, Chen B, Holpfner U, *et al.* (1997) Unimolecular electrical rectification in hexadecylquinolinium tricyanoquinodimethanide. *Journal of the American Chemical Society* 119: 10455.

b0300 48. Horowitz P and Hill W (1989) *The Art of Electronics*. New York: Cambridge University Press.

b0305 49. Sze SM (1981) *Physics of Semiconductor Devices*. New York: Wiley.

b0310 50a. Thurstans RE and Oxley DP (2002) The electroformed metal–insulator–metal structure: A comprehensive model. *Journal of Physics D: Applied Physics* 35: 802.

b0315 50b. Simmons JG and Verderber RR (1967) New conduction and reversible memory phenomena in thin insulating films. *Proceedings of the Royal Society of London Series A* 301: 77.

b0320 50c. Dearnaley G, Stoneham AM, and Morgan DV (1970) Electrical phenomena in amorphous oxide films. *Reports on Progress in Physics* 33: 1129.

b0325 51a. Mann B and Kuhn H (1971) Tunneling through fatty acid salt monolayers. *Journal of Applied Physics* 42: 4398.

b0330 51b. Polymeropoulos EE and Sagiv J (1978) Electrical conduction through adsorbed monolayers. *Journal of Chemical Physics* 69: 1836.

b0335 52. Fan FF, Yang J, Cai L, *et al.* (2002) Charge transport through self-assembled monolayers of compounds of interest in molecular electronics. *Journal of the American Chemical Society* 124: 5550.

b0340 53. Franz W (1956) In: Flugge S (ed.) *Handbuch der Physik* vol. 17, 155p. Berlin: Springer.

b0345 54a. Lewicki G and Mead CA (1966) Experimental determination of *E–k* relationship in electron tunneling. *Physical Review Letters* 16: 939.

b0350 54b. Stratton R, Lewicki G, and Mead CA (1966) The effect of nonparabolic energy bands on tunneling through thin insulating films. *Journal of Physics and of Chemistry Solids* 27: 1599.

b0355 54c. Parker GH and Mead CA (1968) Energy–momentum relationship in InAs. *Physical Review Letters* 21: 605.

b0360 55. Brar B, Wilk GD, and Seabaugh AC (1996) Direct extraction of the electron tunneling effective mass in ultrathin SiO_2. *Applied Physics Letters* 69: 2728.

b0365 56. Joachim C and Magoga M (2002) The effective mass of an electron when tunneling through a molecular wire. *Chemical Physics* 281: 347.

b0370 57. Simmons JG (1963) Generalized formula for the electric tunnel effect between similar electrodes separated by a thin insulating film. *Journal of Applied Physics* 34: 1793.

b0375 58a. Simmons JG (1971) Conduction in thin dielectric films. *Journal of Physics D: Applied Physics* 4: 613.

b0380 58b. Maserjian J and Petersson GP (1974) Tunneling through thin MOS structures: dependence on energy (E–κ). *Applied Physics Letters* 25: 50.

b0385 59a. Yamamoto H and Waldeck DH (2002) Effect of tilt-angle on electron tunneling through organic monolayer films. *Journal of Physical Chemistry B* 106: 7469.

b0390 59b. Napper AM, Liu, Haiying, and Waldeck DH (2001) The Nature of electronic coupling through insulating barriers on Au electrodes. The importance of chain composition and interchain coupling. *Journal of Physical Chemistry B* 105: 7699.

b0395 60a. Lee JO, Lientschnig G, Wiertz F, *et al.* (2003) Absence of strong gate effects in electrical measurements on phenylene-based conjugated molecules. *Nano Letters* 3: 113.

b0400 60b. Haick H, Ghabboun J, and Cahen D (2005) Pd versus Au as evaporated metal contacts to molecules. *Applied Physics Letters* 86: 042113.

b0405 61. Akkerman HB, Blom PWM, de Leeuw DM, and de Boer B (2006) Towards molecular electronics with large-area molecular junctions. *Nature* 441: 69.

b0410 62. González MT, Wu S, Huber R, van der Molen SJ, Schönenberger C, and Calame M (2006) Electrical conductance of molecular junctions by a robust statistical analysis. *Nano Letters* 6: 2238.

b0415 63. Kim T-W, Wang G, Song H, Choi N-J, Lee H, and Lee T (2006) Charge transport of alkanethiol self-assembled monolayers in micro-via hole devices. *Journal of Nanoscience and Nanotechnology* 6: 3487.

b0420 64. Engelkes VB, Beebe JM, and Frisbie CD (2004) Length-dependent transport in molecular junctions based on SAMs of alkanethiols and alkanedithiols: Effect of metal work function and applied bias on tunneling efficiency and contact resistance. *Journal of the American Chemical Society* 126: 14287.

b0425 65. Cui XD, Primak A, Zarate X, *et al.* (2001) Reproducible measurement of single-molecule conductivity. *Science* 294: 571.

b0430 66. Lörtscher E, Weber HB, and Riel H (2007) Statistical approach to investigating transport through single molecules. *Physical Review Letters* 98: 176807.

b0435 67. Hu Y, Zhu Y, Gao H, and Guo H (2005) Conductance of an ensemble of molecular wires: A statistical analysis. *Physical Review Letters* 95: 156803.

b0440 68. Kushmerick JG (2005) Metal–molecule contacts. *Materials Today* 8: 26.

b0445 69. Salomon A, Cahen D, Lindsay S, Tomfohr J, Engelkes VB, and Frisbie CD (2003) Comparison of electronic transport measurements on organic molecules. *Advanced Materials* 15: 1881.

b0450 70. All of these lengths were determined by Chem3D software.

b0455 71a. Beebe JM, Engelkes VB, Miller LL, and Frisbie CD (2002) Contact resistance in metal–molecule–metal junctions based on aliphatic SAMs: Effects of surface linker and metal work function. *Journal of the American Chemical Society* 124: 11268.

b0460 71b. Kaun C-C and Guo H (2003) Resistance of alkanethiol molecular wires. *Nano Letters* 3: 1521.

b0465 72. Bryant MA and Pemberton JE (1991) Surface Raman scattering of self-assembled monolayers formed from 1-alkanethiols: Behavior of films at gold and comparison to films at silver. *Journal of the American Chemical Society* 113: 8284.

b0470 73. Kato HS, Noh J, Hara M, and Kawai M (2002) An HREELS study of alkanethiol self-assembled monolayers on Au(111). *Journal of Physical Chemistry B* 106: 9655.

74. Castiglioni C, Gussoni M, and Zerbi GJ (1991) Charge mobility in s-bonded molecules: The infrared spectrum of polymethylene chains in the solid and liquid phases. *Chemical Physics* 95: 7144. b0475

75. The symbols, δ, γ, and ν denote in-plane rocking (r) and scissoring (s), out-of-plane wagging (w) and twisting (t), and stretching modes, respectively. b0480

76a. Molinari M, Rinnert H, Vergnat M, and Weisbecker P (2003) Evolution with annealing treatments of the size of silicon nanocrystallites embedded in a SiN_x matrix and correlation with optical properties. *Materials Science and Engineering: B* 101: 186. b0485

76b. Bogdanoff PD, Fultz B, and Rosenkranz S (1999) Vibrational entropy of $L12Cu_3Au$ measured by inelastic neutron scattering. *Physical Review B* 60: 3976. b0490

76c. Mazur U and Hipps KW (1982) Spectroscopic characterization of tricyanovinyl alcoholate and pentacyanopropenide salts in solid, solution, and adsorbed phases: NMR, IR, Raman, and tunneling spectra. *Journal of Physical Chemistry* 86: 2854. b0495

77a. Mazur U and Hipps KW (1981) Characterization of alumina supported O_ySiH by inelastic electron tunneling spectroscopy. *Journal of Physical Chemistry* 85: 2244. b0500

77b. Kurata H, Hirose M, and Osaka Y (1981) Wide optical-gap, photoconductive a-Si_xN_{1-x}:H. *Japanese Journal of Applied Physics* 20: L811. b0505

78. Kushmerick JG, Lazorcik J, Patterson CH, Shashidhar R, Seferos DS, and Bazan GC (2004) Vibronic contributions to charge transport across molecular junctions. *Nano Letters* 4: 639. b0510

79. Kirtley J and Hall JT (1980) Theory of intensities in inelastic-electron tunneling spectroscopy orientation of adsorbed molecules. *Physical Review B* 22: 848. b0515

80. Lauhon IJ and Ho W (1999) Single-molecule vibrational spectroscopy and microscopy: CO on Cu(001) and Cu(110). *Physical Review B* 60: R8525. b0520

81. Klein J, Léger A, Belin M, Défourneau D, and Sangster MJL (1973) Inelastic-electron-tunneling spectroscopy of metal–insulator–metal junctions. *Physical Review B* 7: 2336. b0525

82. Lauhon LJ and Ho W (2001) Effects of temperature and other experimental variables on single molecule vibrational spectroscopy with the scanning tunneling microscope. *Review of Scientific Instruments* 72: 216. b0530

83. Kastner MA (1993) The quantum dot: A journey into the future of microelectronics. *Physics Today* January. 24–31. b0535

84. Aviram A and Ratner M (eds.) (1998) *Molecular Electronics: Science and Technology, The Annals of the New York Academy of Sciences,* vol. 852. New York: New York Academy of Sciences. b0540

85. Reimers J, Picconatto C, Ellenbogen J, and Shashidhar R (2003) *Molecular Electronics III, The Annals of the New York Academy of Sciences*, vol. 1006. New York: New York Academy of Sciences. b0545